2017

Spray-Deposited Titanium-Oxide Films For Infrared Optics, Photonics, And Solar Cell Applications.

Sarmad Alhasan
University of Central Florida

SPRAY-DEPOSITED TITANIUM-OXIDE FILMS FOR INFRARED OPTICS, PHOTONICS, AND SOLAR CELL APPLICATIONS

by

SARMAD FAWZI HAMZA ALHASAN
B.Sc. in Electrical & Electronics Eng./Laser Eng.,University of Technology, IRAQ, 2003
M.Sc. in Laser & Optoelectronics Eng./Laser Eng.,University of Technology, IRAQ, 2008

A dissertation submitted in partial fulfilment of the requirements
for the degree of Doctor of Philosophy
in the Department of Electrical and Computer Engineering
in the College of Engineering and Computer Science
at the University of Central Florida
Orlando, Florida

Summer Term
2017

Major Professor: Robert E. Peale

ABSTRACT

Self-assembled TiO_2 foam-like films, were grown by the water based Streaming Process for Electrodeless Electrochemical Deposition (SPEED). The morphology of the $\sim$1 μm thick films consists of a tangled ropy structure with individual strands of $\sim$ 200 nm diameter and open pores of 0.1 to 3 micron dimensions. Such films are advantageous for proposed perovskite solar cell comprising $CH_3NH_3PbI_3$ absorber with additional inorganic films as contact and conduction layers, all deposited by SPEED. Lateral film resistivity is in the range 20 - 200 kΩ-cm, increasing with growth temperature, while sheet resistance is in the range $2 - 20 \times 10^8$ Ω/Sq. Xray diffraction confirms presence of TiO_2 crystals of orthorhombic class (Brookite). UV-vis spectroscopy shows high transmission below the expected 3.2 eV TiO_2 bandgap. Transmittance increases with growth temperature. This is a Ropy TiO_2 thin film.

We also prepared a Smooth TiO_2 thin film. Self-assembled TiO_2 film deposited by aqueous-spray deposition was investigated to evaluate morphology, crystalline phase, and infrared optical constants. The Anatase nano-crystalline film had $\sim$10 nm characteristic surface roughness sparsely punctuated by defects of not more than 200 nm amplitude. The film is highly transparent throughout the visible to wavelengths of 12 μm. The indirect band gap was determined to be 3.2 eV. Important for long-wave infrared applications is that dispersion in this region is weak compared with the more commonly used dielectic SiO_2 for planar structures. The low-cost, large-area, atmospheric-pressure, chemical spray deposition method allows conformal fabrication on flexible substrates for long-wave infrared photonics.

For comparison TiO_2 films deposited by electron-beam evaporation were evaluated to determine morphology, crystalline phase, and optical transparency.

The evaporated TiO_2 film was amorphous but crystallized into Anatase phase after annealing.

Such film is attractive as electron conductor of unprecedented thinness and flexibility for proposed perovskite solar cell comprising $CH_3NH_3PbI_3$ absorber with additional inorganic films as contact and conduction layers. The spray deposition method would allow conformal solar cell fabrication on flexible substrates for wearable power generation. Band gap of Evaporated TiO_2 film is 4.0 eV. We prepared $BaTiO_3$ thin film to know infrared pyroelectric response.

Self-assembled nano-crystalline $BaTiO_3$ films on stainless steel foil substrates, were grown by the water based Streaming Process for Electrodeless Electrochemical Deposition (SPEED). SPEED is an aqueous process that deposits self-assembled nano-crystalline inorganic thin films over large areas, without a vacuum, providing a scalable and manufacturing friendly process to fabricate durable films. The morphology of the $\sim 1\mu$m thick films comprises single crystals of micron dimensions imbedded in a matrix of nanocrystals. XRD confirms presence of $BaTiO_3$ crystals of hexagonal phase for samples annealed at 500°C. Subsequent annealing at 600°C transforms the film to the cubic phase. Potential applications include dielectric layers, capacitors, waveguides, ferroelectric RAM, pyroelectric infrared detectors, and phosphors. Characterization of infrared pyroelectric response at 10μm wavelength shows an initially good sensitivity that reversibly decays over a period of days due to water vapor absorption. A short-lived photo-response due to poling of the hydrated sample is also observed. We studied $BaTiO_3$ to know hysteresis loop.

Pyroelectric photoresponse of aqueous spray deposited thin films containing $BaTiO_3$ nano-crystals is reported. X-ray diffraction data indicate the presence of hexagonal $BaTiO_3$ nano-crystals with $\sim$20 nm crystalline domains in a matrix of some as yet unidentified nano-crystalline material. When the film is annealed at 600°C, the X-ray pattern changes significantly and indicates a conversion to one of the non-hexagonal phases of $BaTiO_3$ as well as a complete change in the matrix. With suitable amplifier, the measured photoresponse was 40V/W.

Ferroelectric hysteresis on a film with significant presence of hexagonal $BaTiO_3$ shows saturated polarization which is about 5-times smaller than for the bulk tetragonal phase.

It is our genuine gratefulness and warmest regard that we dedicate this work to my country IRAQ (Mesopotamia), Higher Committee for Education Development in Iraq (HCED), my father, my mother, my wife, my kids, my brothers, my sister, who are close to me, and close to my family.

ACKNOWLEDGMENTS

First, and foremost, all praise, thanks, and glory goes to Allah through holy Prophet Muhammad, and his Household for their inspiration, persistent generosity, and blessings. They have been my strength when I was weak, my endurance when I was tired, my wisdom when I lacked it, my confidence when I failed, and my joy when I could see result.

University of Central Florida (UCF) for me has been a long journey, and along the way there were a handful of people who played a significant role in me achieving my goal.

Then, words cannot describe the gratitude that I have for my supervisor Professor Robert Edwin Peale. I would like to convey my deep gratitude, and appreciation to him, for accepting me in his group in August 2015. He has been a great support to me for all levels, for his peerless encouragement, and guidance. Even if I made mistakes in the beginning of my Doctor of Philosophy (PhD), he never judged me strictly but continued to provide me with guidance, and ample of time to let me learn to be an independent researcher. I will continue to follow work ethics, and leadership qualities that I have learnt from him in my future efforts.

In addition, he generously sent to me on multiple occasions to the Materials Characterization Facility (MCF) at UCF to take advantage of the available facilities at MCF, and NanoSpective, Incorporated (Inc). Professor Peale was always available for valuable discussions, advice, and guidance. I am very thankful to him, and cherish the chance he gave me. I wished I knew him before that time. I hope that I will continue to work with him in the future.

As well, I would like to thank Dr. Isaiah O. Oladeji, Chief Technology Officer (CTO) at SISOM Thin Films Limited Liability Company (LLC) for his massive contribution to this work, and in providing his skill in fabrication of numerous thin-film some investigated in in this dissertation.

Also, I would like to express my thanks, and appreciation to my Co-advisor Professor Kalpathy B. Sundaram for his support, and guidance.

Then, I would also like to thank my committee members: Professor Aravinda Kar, Professor Wasfy B. Mikhael, and Dr. Reza Abdolvand for their advice, and wisdom in my defense day.

In addition, I also acknowledge to Mr. Kirk Scammon his help in Scanning Electron Microscope (SEM) imaging, and X-Ray Diffraction (XRD) analysis at MCF at UCF. Also, I would like to thanks Ms. Karen Glidewell at MCF at UCF.

Also thanks to Dr. Brenda Prenitzer, Chief Executive Officer (CEO), and President of NanoSpective, Inc. who gave me chance to work with Dr. Imen Rezadad. I would like to express a special thanks to Dr. Rezadad for helping me with Polishing setups, SEM imaging, and his constant guidance toward my experimental.

Then, I would also wish to thank Mr. Austin Elledge, and Mr. Eric Finch at National Instruments (NI) Corporation for helping me in NI USB-6009 setups.

I would also like to thank Mr. Joe Evans at Radiant Technologies, Inc. for helping me in Hysteresis Loop, and Sawyer Tower Circuit.

As well, I would like to extend my hearty thanks to Mr. Christopher Fredricksen for helping me with the Laboratory Virtual Instrument Engineering Workbench (LabVIEW)-controlled setups, and his constant guidance toward experimental work in Dr. Peales laboratories (Infrared Spectroscopy, and MicroDevice Prototyping Facility (MPF)). In addition, I would like to thank to Mr. Christopher, Mr. Doug Maukonen, and Robert Wong helped me making experimental parts at the Physics Machine Laboratory.

As well, I especially would like to thank Mr. Hussain Abouelkhair for helping XRD analysis, SEM imaging, and annealing (Furnace). Also, he helped me for cutting samples at Ara Dr. Research Facility (Laboratory Dr. An).

I particularly would like to thank Mr. Seth Calhoun, and Vanessa Lowry in the UCF Physics Cleanroom for their help me in E- beam evaporated. In addition, Vanessa helped me to measurement thickness of samples by Profilometer.

Then, I would like to extend warm wishes, and multitude of thanks to Dr. Janardan Nath to helping me to samples analysis by using UV-Vis Spectrometer.

In addition, I would like to thank Dr. Farnood Khalilzadeh Rezaie for helping me with Optical Microscope setups.

Also, I would like to thank Mr. Chris Coleman for helping me with Atomic force Microscope (AFM) setups.

As well, I am also thankful of UCF College of Graduate Studies, and UCF Student Government Association (SGA) for providing me travel funds.

Then, I would like to extend my hearty thanks to all the present, and past teachers, and staff members in UCF for their guidance, and help in sorting out the executive aspects of my degree.

In addition, I would like to extend my hearty thanks to all the present, and past teachers, and friends in Preschool, Primary School, Secondary School, College, and University for their guidance, and support.

As well, I would like to acknowledge my fellow group-mates, and friends over the past few years.

Then, I would like to extend my hearty thanks to my Iraqi group-mates, and friends over the past five years for helping my family, and me.

Also, I wish to acknowledge my government, and the program Higher Committee for Education Development in Iraq (HCED), Prime Minister Office, Baghdad, IRAQ, http://hcediraq.org/ for supporting me during all these years, and giving me the opportunity to advance my academic career in the United States America (USA).

Then, I would like to express my deepest gratitude, and appreciation to my father, my mother, and who are close to my family, and me whose have offered everything to me to reach this point in my life. I would like to express my sincere love, and gratitude to my brothers, and sister. Their encouragement, and support are unbounded.

In addition, I would like to express my deepest gratitude, and thanks to my wife for going through this process with me, and putting up with me. This dissertation is as much yours as it is mine. You have stood beside me in all of this, and given me the confidence, and motivation to complete this work.

Finally, thanks as well to my kids who were always there to remind me of the more important things in life. No matter how difficult the day may have been, it was always made better by coming home, and hearing a joyful cry of Baba!

Sarmad

June 06/30/2017

Friday

TABLE OF CONTENTS

LIST OF FIGURES

LIST OF ABBREVIATIONS

AFM . . . . . Atomic Force microscopy

ALD . . . . . Atomic Layer Deposition

CD . . . . . Conduction Band

CNC . . . . . Conduction Computer numerical control

EDS . . . . . Energy Dispersive Spectroscopy

ESL . . . . . Electron selective layers

FIB . . . . . Focus Ion Beam

HSL . . . . . Hole selective layers

LED . . . . . light-Emitting Diode

LWIR . . . . . Long-Wave Infrared

ICDD . . . . . International Centre for Diffraction Data

MCF . . . . . Materials Characterization Facility

PSC . . . . . Perovskite Solar Cells

PCE . . . . . Power conversion efficiencies

RAM . . . . . Random-Access Memory

SEM . . . . . Scanning electron microscopy

SPEED . . . . . Streaming Process for Electrodeless Electrochemical Deposition

VPSPEED. . . . . Vapor Phase Streaming Process for Electrodeless Electrochemical Deposition

CHAPTER 1: INTRODUCTION

Performance of Perovskite Solar Cells (PSC) has advanced rapidly[1, 2, 3, 4, 5, 6]. Perovskites are compounds of the form ABO_3. Solar Cells based on spin-coated mesoporous TiO_2 scaffold, $CH_3NH_3PbI_3$ perovskite absorber layer, and a 2, 2, 7, 7- tetrakis-(N, N-di-p-methoxyphenylamine)-9, 9-bifluorene (spiro-OMeTAD) hole transport layer have been reported with Power Conversion Efficiency (PCE) as high as 15%, and with 20% considered achievable. However, mesoporous TiO_2 as a conducting layer has demonstrated poor quality and poor electron conduction [7]. We present here a robust foam-like TiO_2 film grown by a water-based process that can be a superior alternative. Similarly, the organic spiro-OMeTAD used previously as hole conductor has poor hole transport. Instead, durable films of CuS with excellent hole transport grown by our same aqueous process might be substituted [8, 9].

Titanium dioxide is a very well-studied material with wide ranging applications, including electron collector in solar cells [10, 11, 12, 13], optical waveguides [14], optical coatings [15], polarized [16], ultra-thin capacitors [17], corrosion-barriers [18], protective coatings [19], MOSFETs [20], humidity sensors [21], and oxygen monitors [22]. Enabling features of TiO_2 include excellent visible transmittance, chemical stability, high permittivity [23], mechanical durability, high electrical resistance [24], and rigidity [25]. This work considers a Smooth TiO_2 as a potential useful material for long-wave infrared (LWIR) photonics applications. This consideration is motivated by the relatively low dispersion for TiO_2 in the 8 to 12μ m wavelength range, in comparison to SiO_2, which is the most common dielectric in devices fabricated by silicon processing.

An additional motivation for this work is to evaluate a potentially advantageous aqueous deposition method that provides smooth conformal coatings. Titanium dioxide TiO_2 exists in nature as the minerals Rutile (tetragonal), Anatase (tetragonal) and Brookite (orthorhombic). Many factors affect the crystalline phase of deposited TiO_2 thin films, including deposition method, deposition temperature, annealing temperature, deposition rate, deposition pressure, precursor type, reaction atmosphere, impurities, and substrate type. TiO_2 films have been deposited by many different techniques, including hydrolysis [26], pyrolysis [27], pneumatic spraying [28], ultrasonic spraying [29], dip coating [30], plasma enhanced chemical vapor deposition [31], atmospheric pressure chemical vapor deposition [32], metal organic chemical vapor deposition [33], ultra high vacuum chemical vapor deposition [34], low pressure chemical vapor deposition [35], evaporation [36], spin on methods [37], sputtering [38], ion assisted deposition [38], plasma anodization [39], reactive ion plating [40], laser ablation [41], filtering arc deposition [25], atomic layer epitaxy [42], and screen printing [43]. The complex refractive index spectra of TiO_2 thin films prepared by atomic layer deposition (ALD) [44] and by reactive sputter deposition [45] have already been reported out to far infrared wavelengths (125μ m). Both films were prepared by vacuum-based physical deposition methods. The atmospheric-pressure aqueous inhomogeneous-chemical reaction-based deposition method investigated here has the potential for much lower cost, large area, perfectly conformal [46, 47] roll-to-roll manufacturing. Physical and optical properties of these films are investigated in this work with particular emphasis on application to infrared photonics, such as metal-insulator-metal plasmonic resonant absorbers [48] and planer waveguides [49].

The inorganic compound barium titanate ($BaTiO_3$) is a member of the Perovskite family, which has the general formula ABO_3. $BaTiO_3$ has excellent dielectric, ferroelectric and piezoelectric properties. $BaTiO_3$ was the first ferroelectric ceramic, and it is a good candidate for a diverse applications due to its high permittivity and low loss [50].

Applications include pyroelectric detectors [51], capacitors [52], waveguide modulators [53], gate dielectrics [54] and holographic memory [55].

The optimum synthesis method for $BaTiO_3$ depends on the end application, as the method used has a significant impact on the structure and properties of $BaTiO_3$. Its five known phases are hexagonal, cubic, tetragonal, orthorhombic, and rhombohedral. This work considers the pyroelectric response to infrared radiation of $BaTiO_3$ thin films.

Pyroelectric response is the generation of small voltage difference across opposite faces of the film due to a change in temperature that changes the films intrisic polarization. Of its 5 possible crystal classes, only the cubic phase is incapable by symmetry of being pyroelectric [56]. Methods of preparing $BaTiO_3$ include solid-state reaction [57], chemical methods [58], hydrothermal growth [59], sol-gel processing [60], spray pyrolysis [61], the oxalate route [62], microwave heating [28], a micro-emulsion process [63] a polymeric precursor method [64], nanometer oxides doping [63] and modified combustion process [65]. We present a different method of thin film preparation, which is superficially similar to spray pyrolysis, except that it does not involve thermal splitting of molecules, and hence operates at lower temperature.

Motivation for the subject research is to develop an in-house IR detector material that can be deposited, patterned, and integrated with on-chip infrared photonic and plasmonic devices, such as spectral sensors [49, 66]. Barium titanate ($BaTiO_3$) was selected because this well-known ferroelectric material is amenable to our spray deposition technique, known as Streaming Process for Electrodeless Electrochemical Deposition (SPEED). SPEED is superficially similar to spray pyrolysis, except that it does not involve thermal splitting of molecules, and hence operates at lower temperature. SPEED results in perfectly conformal nano-crystalline thin films with strong adhesion [10, 67, 68]. Pyroelectric photoresponse of SPEED grown $BaTiO_3$ thin films was first reported in ref [69].

A purpose of the present work is to further investigate this response and the dependence of materials properties on processing conditions. SPEED deposits inorganic thin films over large areas, without a vacuum, a scalable and manufacturing friendly process.

Water-soluble compounds with complexing agents grow films by heterogeneous reaction on the substrate, with little wasteful homogeneous reaction. Hydrophilic substrates bind hydroxyl ions, which serve as attachment and nucleation sites with density exceeding $10^{12} cm^{-3}$. The nebulized aqueous precursor impinges on a substrate heated to $\sim 300^{\circ}$C, giving growth rate exceeding 200 nm/min. Substrate heating provides reaction activation energy, and it decomposes and volatilizes reaction byproducts.The five known phases of bulk crystalline $BaTiO_3$ are hexagonal, cubic, tetragonal, orthorhombic, and rhombohedral. Tetragonal is the stable phase at room temperature. The cubic phase exists above the 120°C Curie Temperature. The high temperature hexagonal phase can be meta-stable at room temperature. The orthorhombic and rhombohedral phases occur at lower temperatures. All but the cubic phase are capable of a pyroelectric photoresponse [56], which is the appearance of a small voltage difference across opposite faces of the material due to a temperature-induced change in the films intrinsic polarization. The actual stable phase of $BaTiO_3$ film at room temperature can differ from that of crystal due to interaction with the substrate, and it can depend on processing history. We previously reported both cubic and hexagonal phase for room temperature SPEED-grown $BaTiO_3$ thin films [69].

CHAPTER 2: EXPERIMENTAL METHODS

2.1 Experimental Methods for Ropy TiO_2 for Solar Cells

Our aqueous process is called Streaming Process for Electrodeless Electrochemical Deposition, or SPEED. This method deposits self-assembled nanocrystalline inorganic thin films over large areas without vacuum. Water-soluble compounds with complexing agents grow films by heterogeneous reaction on the substrate, with little wasteful homogeneous reaction. Hydrophilic substrates bind hydroxyl ions $(OH)^-$, which are attachment sites for nucleation with density exceeding $10^{12} cm^{-3}$. The substrate is heated to provide at least the reaction activation energy. With these films, the photovoltaic cell comprising glass / SnO_2:F / TiO_2 / $CH_3NH_3PbI_3$ / CuS / Mo can be prepared as shown in figure 2.1-a. Figure 2.1-b presents an optical microscope image of a multilayer film comprising Na Glass substrate, SnO_2:F transparent conducting oxide, TiO_2:Ni, and Ni. This sample was annealed at $270°$C. The image reveals significant porosity with a length scale of 10s of microns. In films grown at higher temperature, this microstructure was less pronounced.

Photo-generated electrons in the perovskite absorber layer would be injected into the embedded TiO_2 wires that would transport these electrons to the transparent-conducting SnO_2:F electrode [67]. Photo-generated holes would be injected into the inorganic CuS hole layer with transport to the Mo electrode.

Since the TiO_2 lies above the perovskite absorber layer, it must have high transparency in the visible range while maintaining sufficiently high electron conductivity.

Glass
Al_2O_3 (Alumina)
TCO (Transparent-Conductive-Oxide)
TiO_2 (Titanium Dioxide)
$CH_3NH_3PbI_3$
CuS (Copper Sulfide)
Mo (Molybdenum)

(a)

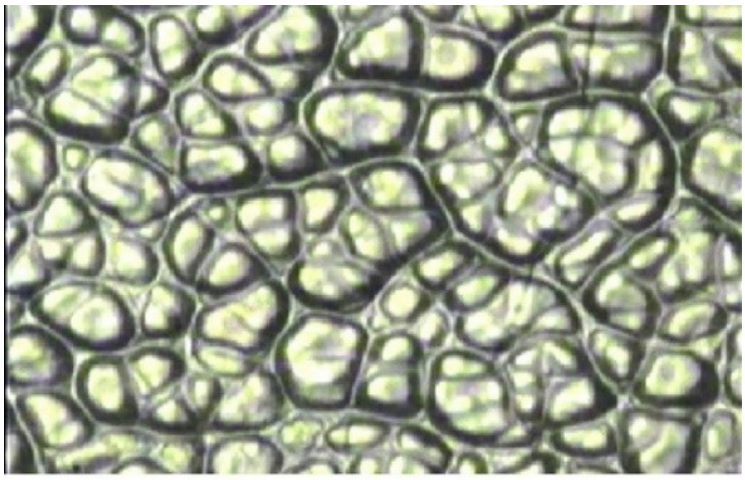

(b)

Figure 2.1: Figure 2.1-a is a schematic of proposed Perovskite Solar Cell layer structure. Figure 2.1-b is an optical microscope image of SPEED-grown TiO_2 thin film.

Borofloat glass substrates were cleaned using a heavy-duty degreaser, acetone, and de-ionized water. Then, the substrate was mounted on a heater set to the growth temperature between $270°$C and $400°$C with $\sim 10°$C uncertainty. The SPEED version used here is vapor phase SPEED (VP-SPEED). The water-based precursor is nebulized into 10 to 20 μm droplets, which are sprayed onto the substrate. Growth rate exceeds 200 nm per minute. Reaction byproducts are decomposed and volatilized. A computer controls the position of the spray nozzle on a 2-axis CNC machining table. Five spray cycles were made for each sample. Annealing was performed for 10 minutes in a tube furnace preheated to $450°$C . Scanning electron microscopy (SEM, Zeiss ULTRA-55) with Energy Dispersive Spectroscopy (EDS) was performed at the UCF Materials Characterization Facility (MCF). For cross-sectional SEM imaging, samples were cut and their edges polished. Asymmetric out-of-plane X-ray Diffraction (XRD) was measured using PANalytical Empyrean. The incidence angle with respect to the sample plane was 1 degree. The X-ray wavelength was Cu K-Alpha 1, 0.1540598 nm. Optical microscopy was performed using a Nikon Labophot Microscope.

In-plane resistivity was measured using a 4-point probe. Resistivity normal to the plane was determined by measuring the I-V curve via a $1cm^2$ evaporated Ni contact. A Cary 500i spectrophotometer was used to measure film transmittance spectra using bare substrates in the reference channel.

2.2 Experimental Methods for Smooth TiO_2 for Infrared Total Photonics

Our aqueous process is called Streaming Process for Electrodeless Electrochemical Deposition, or SPEED. The substrate is heated to provide at least the reaction activation energy as shown figure 2.2. Figure 2.2 presents a photograph of the SPEED apparatus during deposition. In contrast to chemical bath deposition, SPEED ensures that films grow by heterogeneous reaction only, instead of a mixture heterogeneous and homogenous reactions.

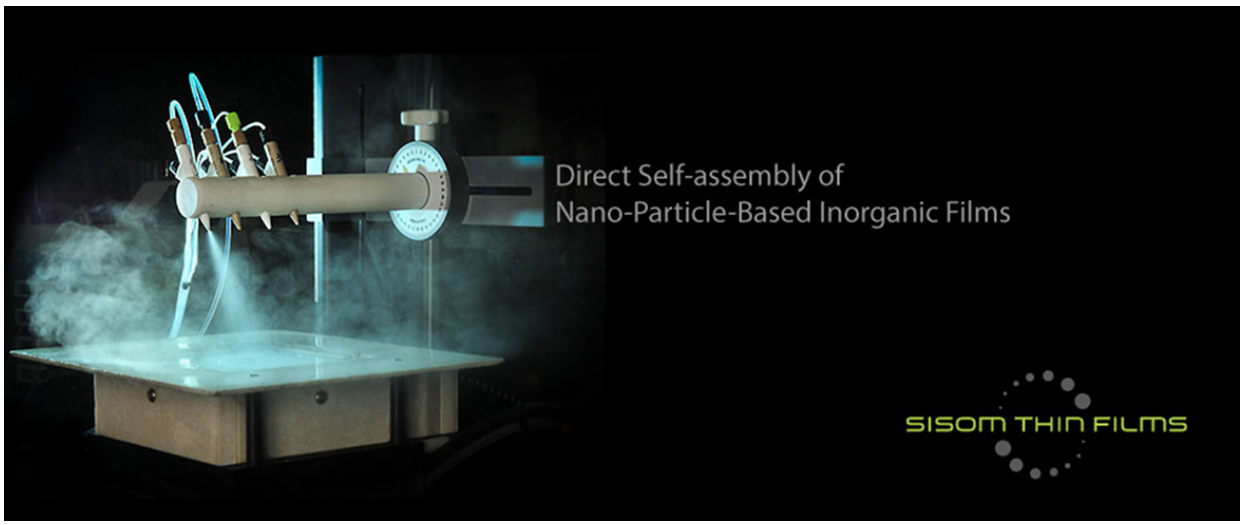

Figure 2.2: SPEED Deposition method

For TiO_2 growth, precursors comprised 0.1 M titanium chloride in mixed water and organic solvents. The 20%-by-volume deionized water is a solvent, provides surface-attached $(OH)^-$, and is the source of oxygen. Organic solvents ethanol, isopropanol, and methyl propanol serve mainly as complexing agents for Ti ions.

We chose silicate glass and aluminum-coated glass surfaces on which to grow films. Both surfaces are hydrophilic and readily anchor hydroxyl ions that serve as nucleation sites. The $(OH)^-$ ions attract positively charged complexes to initiate electrochemical reaction, without external field or electrodes. The heterogeneous chemical reactions are:

$$[Sub](OH)^- + [TiL_n]^{p+(4+)} \rightarrow [Sub]Ti(OH)^{3+} + (L_n)^p \uparrow \tag{2.1}$$

$$[Sub]Ti(OH)^{3+} + 3(OH)^- \rightarrow [Sub]TiO_2 + 2H_2O \uparrow \tag{2.2}$$

where L is the ligand supplied by the organic solvents, $[Sub]$ is the heated substrate, p is the charge of the ligand L, and n is the number of ligands involved in the Ti/L coordination. Up arrows indicate decomposition and evaporation of reaction byproducts. Substrate temperature must exceed the heterogeneous reaction activation energy and be sufficient to eliminate byproducts. Site regeneration follows

$$[Sub]TiO_2 + (OH)^- \rightarrow [Sub]TiO_2(OH)^- \tag{2.3}$$

The freshly attached $(OH)^-$ initiates the next growth cycle. Lateral grain growth competition leads to nanoparticle morphology.

Asymmetric out-of-plane X-ray Diffraction (XRD) was measured using PANalytical Empyrean system. The XRD patterns were measured using CuKα radiation λ= 0.154059 nm at 45 kV and 40 mA with 2θ scanned from 20 to 65 deg. The incidence angle with respect to the sample plane was 1 degree.

These data were compared with reference spectra for Anatase, Rutile and Brookite from International Centre for Diffraction Data (ICDD) PDF2 Release 2015.

Scanning Electron Microscopy (SEM) was performed using Zeiss ULTRA-55. Cross section samples were prepared by standard polishing technique using Allied Multiprep Polishing System-12 and briefly etched in 10:1 Buffered Oxide Etch solution to enhance image contrast. SEM imaging was done using Zeiss Cross Beam Feild Emission Gun (FEG) SEM. Samples for SEM imaging were sputter coated with 2 nm Iridium (Gatan Precision Etching Coating System). Atomic Force Microscopy (AFM) of the TiO_2 films was performed using (DI) Digital Instruments 5000U. Data visualization and analysis used the Gwyddion program. A Cary 500i spectrophotometer was used to measure film-on-glass transmittance spectra. A bare glass substrate was used in the reference channel.

2.3 Experimental Methods for SPEED $BaTiO_3$ for Pyroelectrics

Self-assembled nano-crystalline $BaTiO_3$ films on stainless steel foil substrates, were grown by the water based Streaming Process for Electrodeless Electrochemical Deposition (SPEED). The nebulized aqueous precursor impinges on a substrate heated to $\sim 300^{\circ}$C, giving growth rate exceeding 200 nm/min. Substrate heating provides reaction activation energy and decomposes/volatilizes reaction byproducts at temperatures well below those required for spray pyrolysis. Grown films were subsequently annealed in the range 500-600°C for 1-2 hours. Figure 2.3 presents photograph of experimental set up for photoresponse measurements. Physical characterization by Scanning Electron Microscopy (SEM, Zeiss ULTRA-55 FEG) and asymmetric out-of-plane X-ray Diffraction (XRD, PANalytical Empyrean #2) were performed at the UCF Materials Characterization Facility (MCF). The Cu Kα X-ray beam at 0.1540598 nm was incident at a fixed angle of 1 deg.

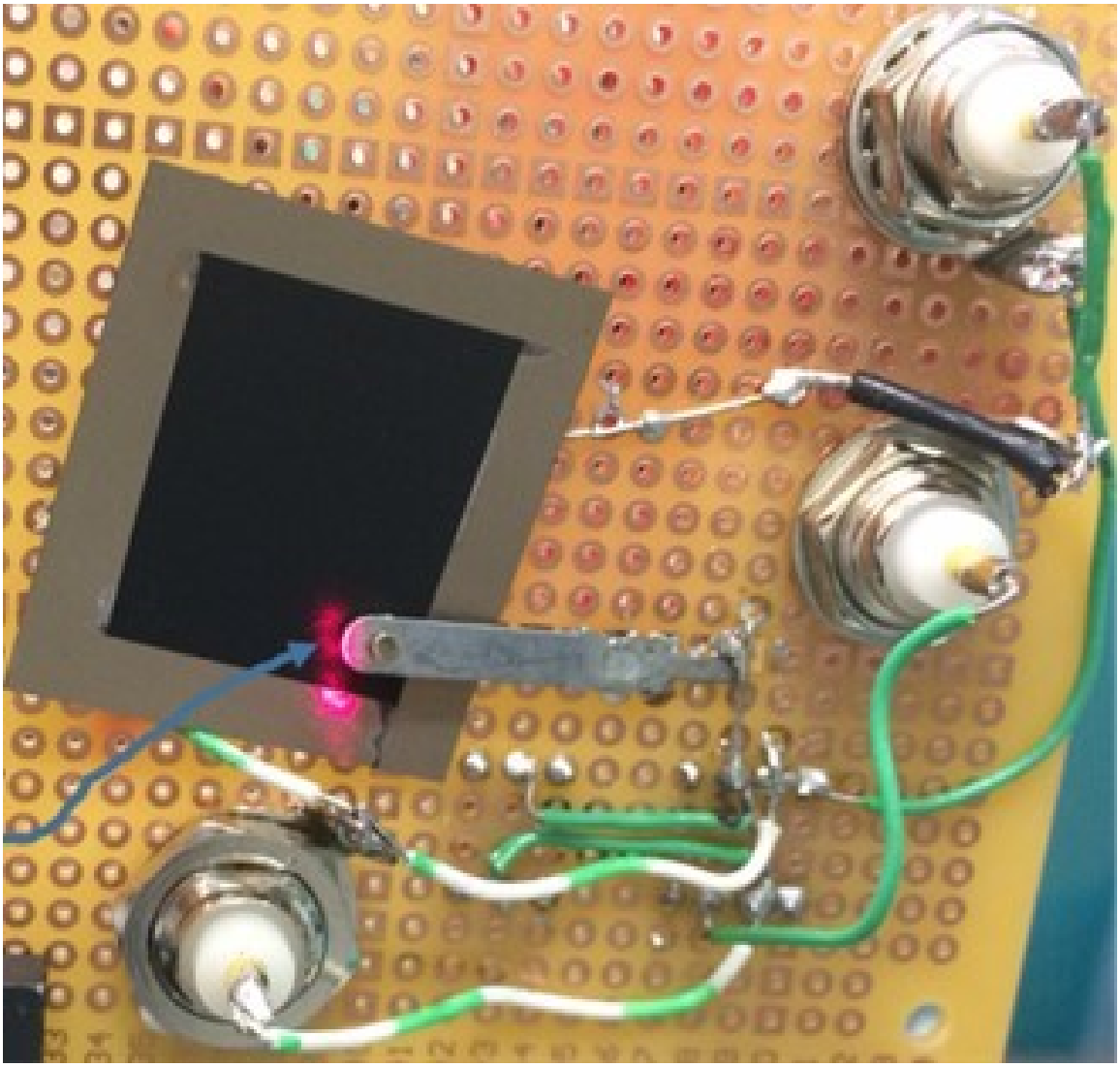

Figure 2.3: Photograph of experimental set up for photoresponse measurements. A spring contact connects to the carbon-black coating on the $BaTiO_3$ thin-film. The amplifier is constructed on the back side of the printed-circuit board. The arrow points to the spot of a red alignment laser which indicates the position illuminated by the pulsed CO_2 laser

In preparation for photo-response measurements, a 4μm thick $BaTiO_3$ film on 75μm thick stainless steel foil substrate, which had been annealed 2 hours at 500°C, was coated with a conducting carbon-black IR absorbing layer.

A gold-coated spring contact was made to the carbon black layer and connected to the inverting input of a type 741 operational amplifier, as shown in figure 2.3. The substrate and non-inverting input of the op-amp were grounded. A 1 MΩ feed-back resistor was connected between inverting input and op-amp output, which was connected to a digital oscilloscope.

Photoresponse was excited using a pulsed CO_2 laser (MTL-3 Mini TEA, Edinburgh Instruments) at 10 micron wavelength. Pulse duration was approximately 100 ns and repetition rate was 2 Hz. The peak power was not precisely measured, but the power in a single pulse was sufficient to cause a noticeable change in the color of liquid-crystal thermal paper designed for 25-30 deg operation (Edmund Optics R25C5W). The color change was similar to that caused by a 100 mW CW CO_2 laser, allowing an estimate of 50 mJ per pulse. This value is the same order as that specified in the laser manual.

The precursor solution included $Ba(NO_2)_2$ and $TiCl_2$ as the source of Ba and Ti ions. The likely reaction is

$$(BaTi) - Ligand^{(p+6)} + substrate - (OH)^- \rightarrow substrate - BaTi(OH)^{5+} + Ligand^{(p)}(gas) \tag{2.4}$$

$$(substrate) - BaTi(OH)^{5+} + 5(OH)^- \rightarrow (substrate) - BaTiO_3 + 3H_2O(gas) \tag{2.5}$$

The superscript p is the ligand charge, which may be positive, negative, or zero. Thirty spray cycles were applied at 300°C , and then the films were annealed at 450 or 500°C for 2 hours. Subsequent annealing at 600°C was also performed on some samples. A purpose of the post growth anneal was to decompose and volatize residual byproducts and recrystallize the formed nanoparticles based film.

Scanning electron microscopy (SEM, Hitachi SU70) with energy dispersive X-ray spectroscopy (EDX) was used for surface and cross sectional imaging and elemental analysis.

Asymmetric out-of-plane X-ray diffraction (XRD, PANalytical Empyrean) was performed to determine crystalline phases. The CuKα X-ray beam at 0.1540598 nm was incident at a fixed angle of ω = 10 deg. The scattered intensity was recorded as a function of scattering angle 2θ. For photo-response measurements, a $\sim$1 μm-thick film on stainless steel substrate was coated with a $\sim$30 μm thick conducting carbon-black IR absorbing layer. Sample area was 1 to 4 cm^2. Photo-response measurements were made using two different IR sources and amplifiers.

System A comprised a CO_2 laser (Access Lasy 3S) with $\sim$100 mW CW power, which was mechanically chopped at 70 Hz. Laser spot size on the sample was $\sim$1-2 mm. A spring contact was made to the carbon black layer and connected to the inverting input of a type 741 operational amplifier with 1 MΩ negative feedback resistor. The substrate and noninverting input of the op-amp were grounded. There was no electronic filtering. A digital oscilloscope averaged 64 traces of the photoresponse.

System B measured pyroelectric current based on the dynamic capacitance method [70]. A broadband black-body source chopped at 1 Hz illuminated the sample with $\sim$13 mW/cm^2. A low-noise high-gain pre-amplifier converted the pyroelectric current into a voltage with gain of 1V/100 pA. The signal was filtered by a 7.2 Hz low-pass. A digital oscilloscope averaged 16 traces.

Ferroelectric hysteresis was measured by the Sawyer Tower method [71]. A sawtooth voltage V_x was applied across the series combination of a capacitor made from our $\sim$1 μm thick film with area A=1 cm^2 and a sense capacitor C_s =1 μF. Since most of V_x is dropped across the much smaller sample capacitor, the electric field in the film is V_x divided by film thickness. The polarization (P) is determined by the extraneous charge on the sample capacitor, which is the same as that on the sense capacitor, so that P = (C_s/A) V_y, where V_y is the voltage dropped on C_s.

CHAPTER 3: RESULTS AND DISCUSSION OF ROPY TiO_2 FOR SOLAR CELLS

Figure 3.1 presents top-view, and cross sectional SEM images of the Ropy TiO_2 film. In top view, the films have a ropy texture, with large surface area.

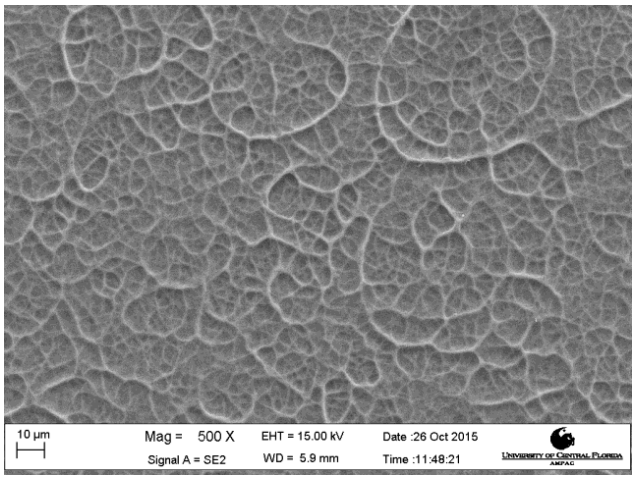

(a)

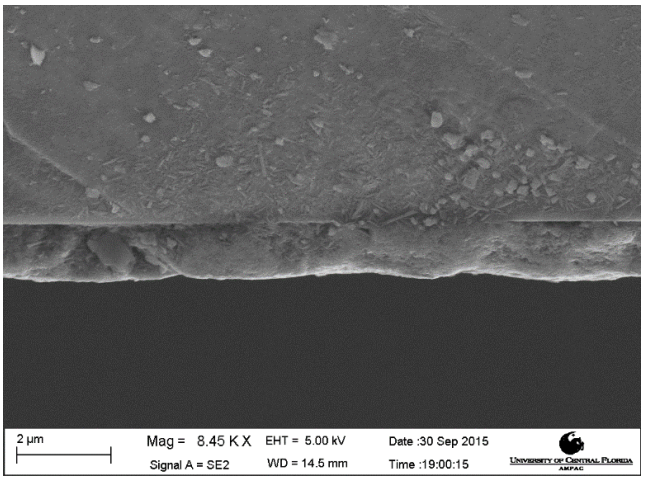

(b)

Figure 3.1: SEM images for TiO2:Ni film. Figure 3.1-a is a top view. Figure 3.1-b is is a cross section.

The cross-section reveals the film thickness to be $\sim 1\mu$m. Energy Dispersive Spectroscopy (EDS) confirms the presence of Ti, O, and Ni in the film. There is 16% as much Ni as Ti in the film, which agrees with the mix in the precursor.

Figure 3.2-a presents example XRD data for one of the films. The growth temperature was $300°$C and sample was not annealed. XRD spectra were collected for all samples, and their XRD patterns were found to be independent of growth temperature and annealing. The spectra were compared with reference spectra for Anatase, Rutile and Brookite (shown) from International Centre for Diffraction Data (ICDD) PDF2 Release 2014. The phase was identified as Brookite (orthorhombic).

Cross sections of all grown samples reveal the layer thickness dependence on growth conditions. Figure (3.2-b, top) presents a plot of film thickness as a function of growth temperature. Post-growth annealing caused no significant difference in the film thickness, so results for annealed and unannealed samples are averaged. For the same 5 spray cycles, the thickness decreases by a factor of $\sim$2 on increasing growth temperature from $270°$ to $400°$C. Figure (3.2-b, bottom) presents the measured in-plane resistivity and sheet resistance as a function of growth temperature. The two curves are not exactly proportional because of differences in film thicknesses for different samples. The resistivity increases with growth temperature and covers the range $40 - 200k\Omega - cm$. In plane conduction less important for solar cell function than vertical transport, since photo-electrons must pass vertically through the TiO_2 layer to reach the Fluoride doped Tin Oxide (FTO) transparent conducting top contact. If the resistivity to vertical transport is the same as the horizontal, we would expect a resistance for $1cm^2$ cross section and 1 micron thickness to be in the range $4 - 20\Omega$. However, the vertical resistance through a Ni pad of this area was found to be 4500Ω, presumably due to high contact resistance.

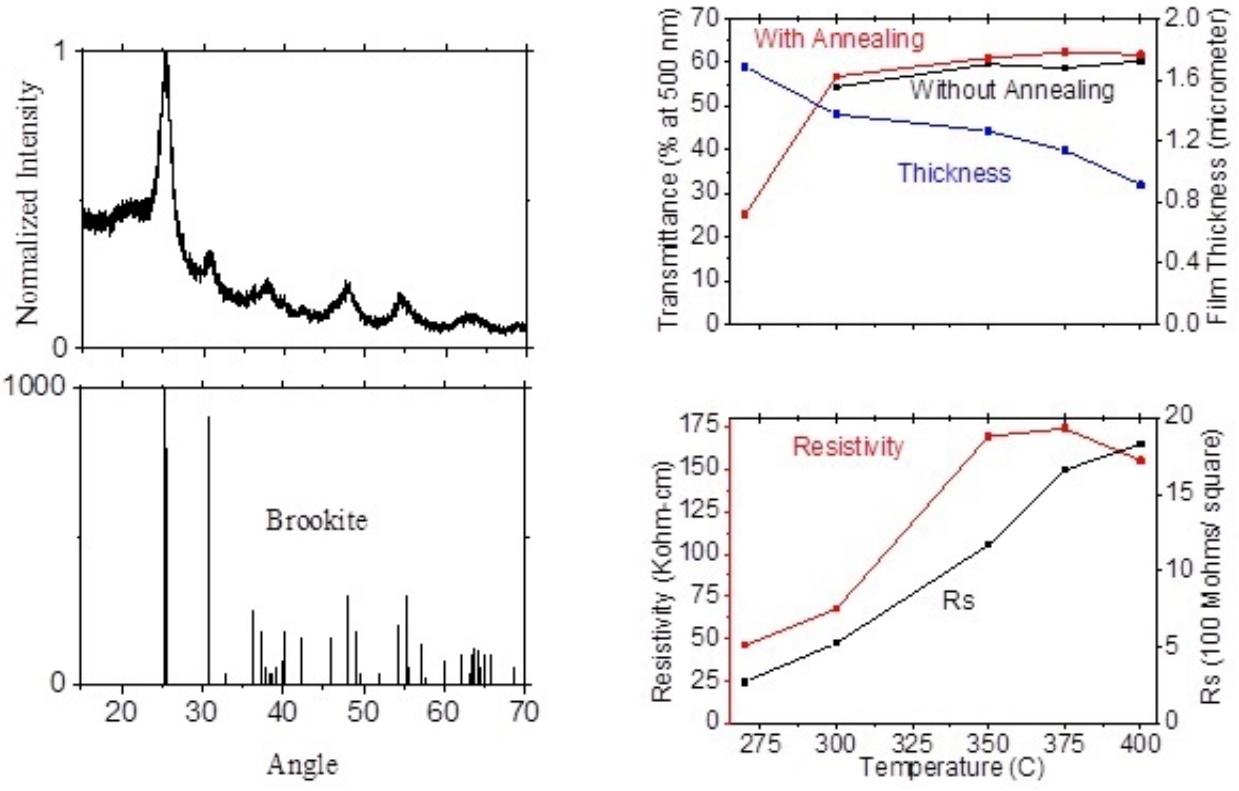

Figure 3.2: Figure 3.2-a is a typical XRD spectrum of SPEED-grown with Brookite phase reference data. Figure 3.2-b is a resistivity, sheet resistance, film thickness, and optical transmittance at 500 nm wavelength versus growth temperature.

The optical transmittance spectra of the films all have the same rapid drop at wavelengths below 388 nm, which corresponds to fundamental absorption above the 3.2 eV TiO_2 bandgap. Transmittance increases with growth temperature as shown in figure (3.2-b, top), which may be reasonably attributed to a combination of the correlated thickness decrease and R_S increase.

CHAPTER 4: RESULTS AND DISCUSSION OF SMOOTH TiO_2 FOR INFRARED TOTAL PHOTONICS

We designate the film considered here as Smooth SPEED TiO_2 to distinguish it from a highly structured film grown by a different SPEED recipe studied earlier[10], which was designated Ropy SPEED according to its observed morphology. Figure 4.1 presents XRD data and shows that Smooth SPEED TiO_2 on Al-coated glass is Anatase phase. (Growth of TiO_2 on a conducting substrate was motivated by certain Long-Wave Infrared (LWIR) applications of interest [50]). This XRD spectrum also shows definitively identified aluminum peaks from the metal coating on the substrate.

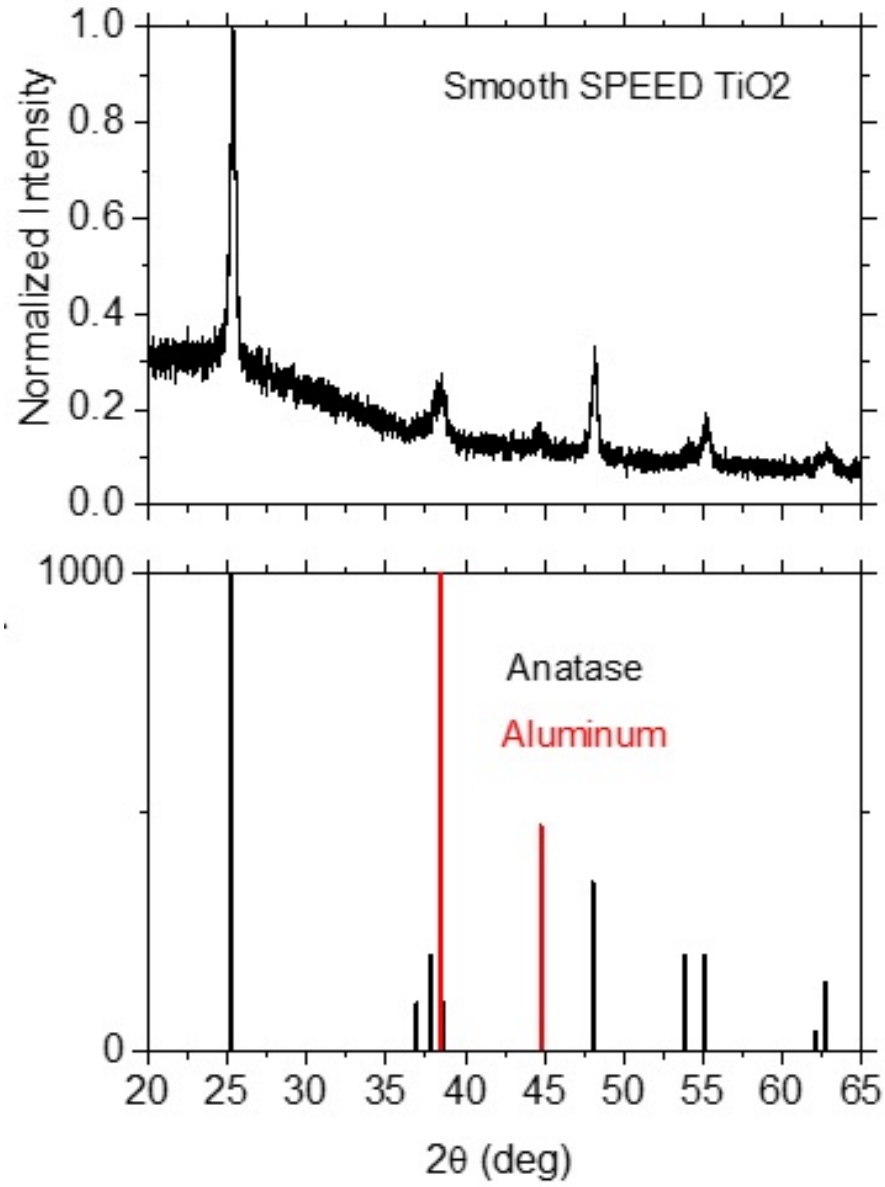

Figure 4.1: XRD Smooth TiO_2 film and reference spectra

Figure 4.2 presents SEM images of the top surface of the film.

The surface is mostly smooth and featureless, except for small scattered blisters, mostly with lateral dimensions of order $\sim 1\mu$m. These films are suitable for long-wave infrared (LWIR) applications, because those wavelengths ($\sim 10\mu$m) are much larger than the surface defects.

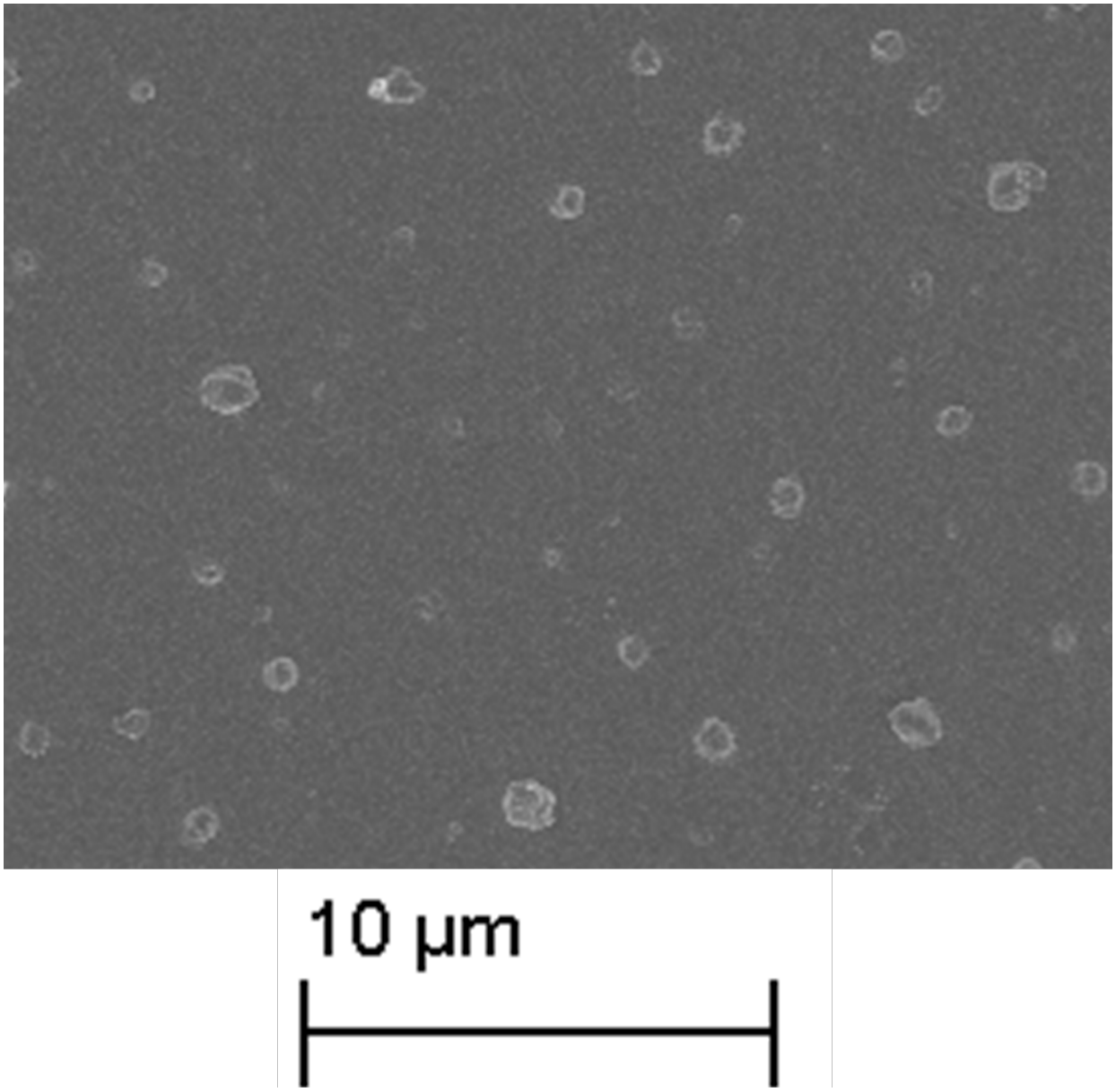

Figure 4.2: SEM image of Smooth SPEED TiO_2 film surface

Figure 4.3 presents SEM cross sections of the film. Substrate, aluminum, TiO_2 layers, and 200 nm scale bar are indicated. The thicknesses of the Smooth SPEED TiO_2 film is approximately 130 nm.

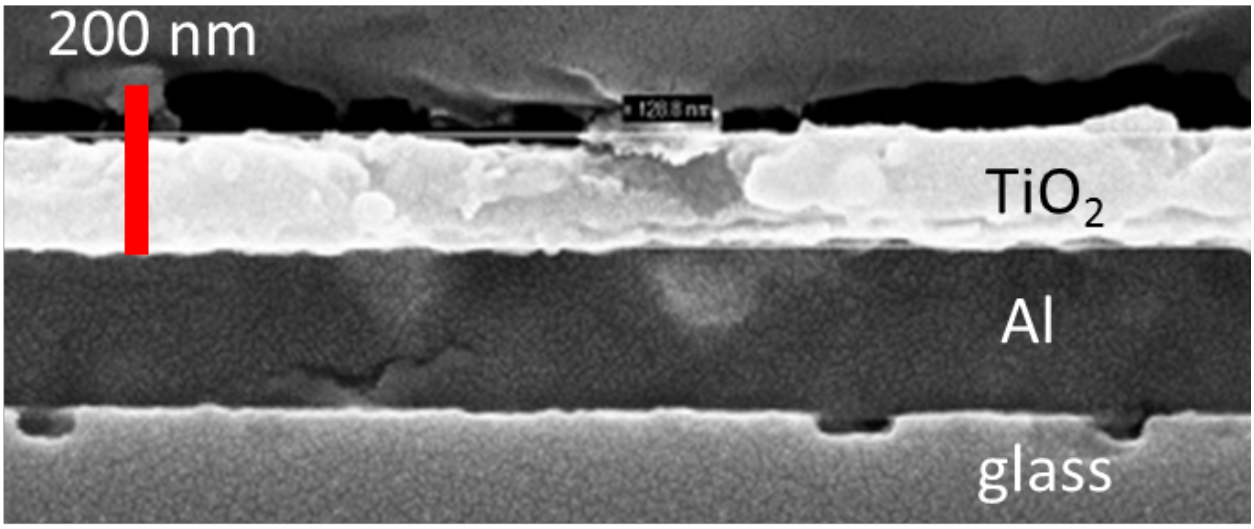

Figure 4.3: SEM cross-sectional image of Smooth SPEED TiO_2 film.

Figure 4.4 presents an AFM image of the Smooth SPEED film sample. The surface is characterized by sparse, isolated, and narrow peaks of $\sim$200 nm amplitude and $\sim$1 μm wide base on a smooth background of $\sim$10nm roughness, which is consistent with the SEM image 4.2.

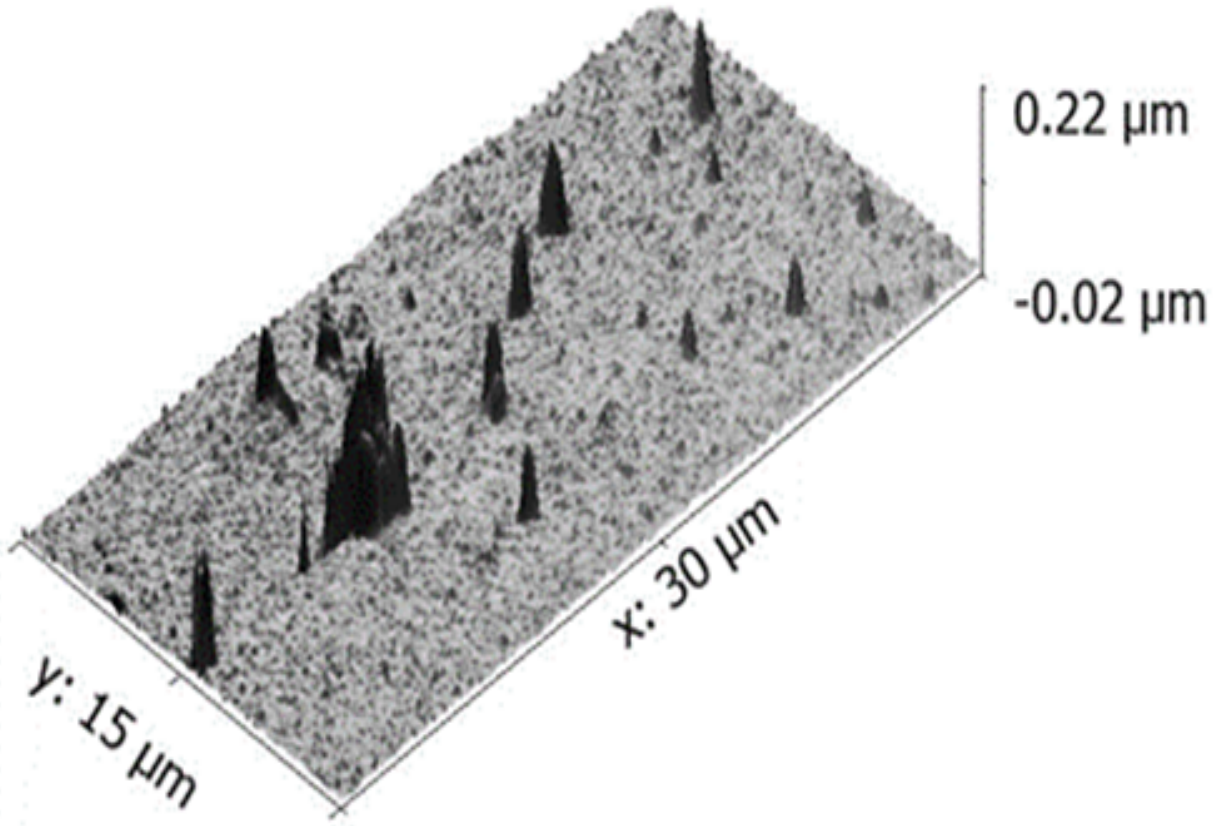

Figure 4.4: AFM images of Smooth SPEED TiO_2.

Figure 4.5 present a UV-visible transmission spectrum for a portion of the film where the substrate was uncoated with Al. The values for the refractive index of anatase at 2.5 eV is $\sim$3 for unpolarized light and random crystallite orientation [72].

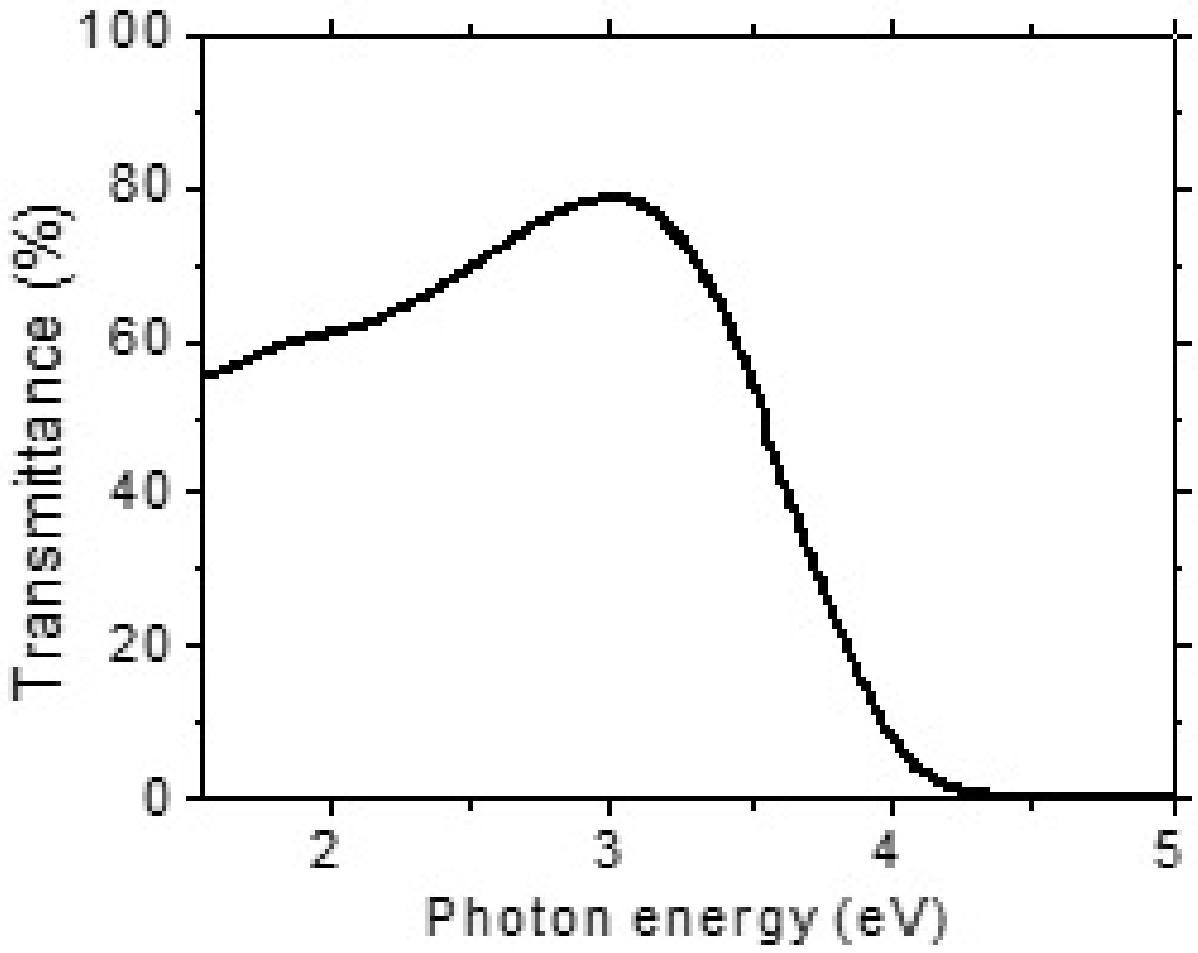

Figure 4.5: Transmission spectrum of Smooth SPEED TiO_2.

Thus, the Fresnel reflectance $R = (n-1)^2/(n+1)^2$ would be 25% at 500 nm wavelength. The peak transmittance at 3 eV is 80%, i.e. larger than expected. This may be a due to optical interference within the high index thin film. At longer wavelengths, where the index is smaller, scattering weaker, and fundamental absorption out of range, we might expect that the transmittance should increase, but the opposite is observed. The optical thickness n×d of the film is $\sim$ 390 nm, which exceeds half the 500 nm wavelength, so that interference in the film can be important. This is supported by the observation of one full Fabry-Perot oscillation period in our transmittance spectrum of a 210 nm thick evaporated TiO_2 film in the same spectral range.

For the thinner Smooth-SPEED film, Fabry-Perot fringes should be separated by 1.5 eV. A weak bump appears in figure 4.5 at 1.2 eV below the 3 eV peak. This might be the Fabry-Perot fringe, since the high frequency side of the 3 eV peak is truncated by fundamental absorption.

Figure 4.6 presents analysis of the UV-visible transmittance spectrum to determine the band gap Eg of the film. The absorption coefficient α was calculated according to Beers law $(1/d)\ln[1/T)]$ from film thickness d and the transmittance spectrum T, which was first normalized to remove the Fresnel reflectance factor. Anatase is an indirect gap semiconductor [72], whose absorption edge depends on absorption and emission of phonons, according to [73]

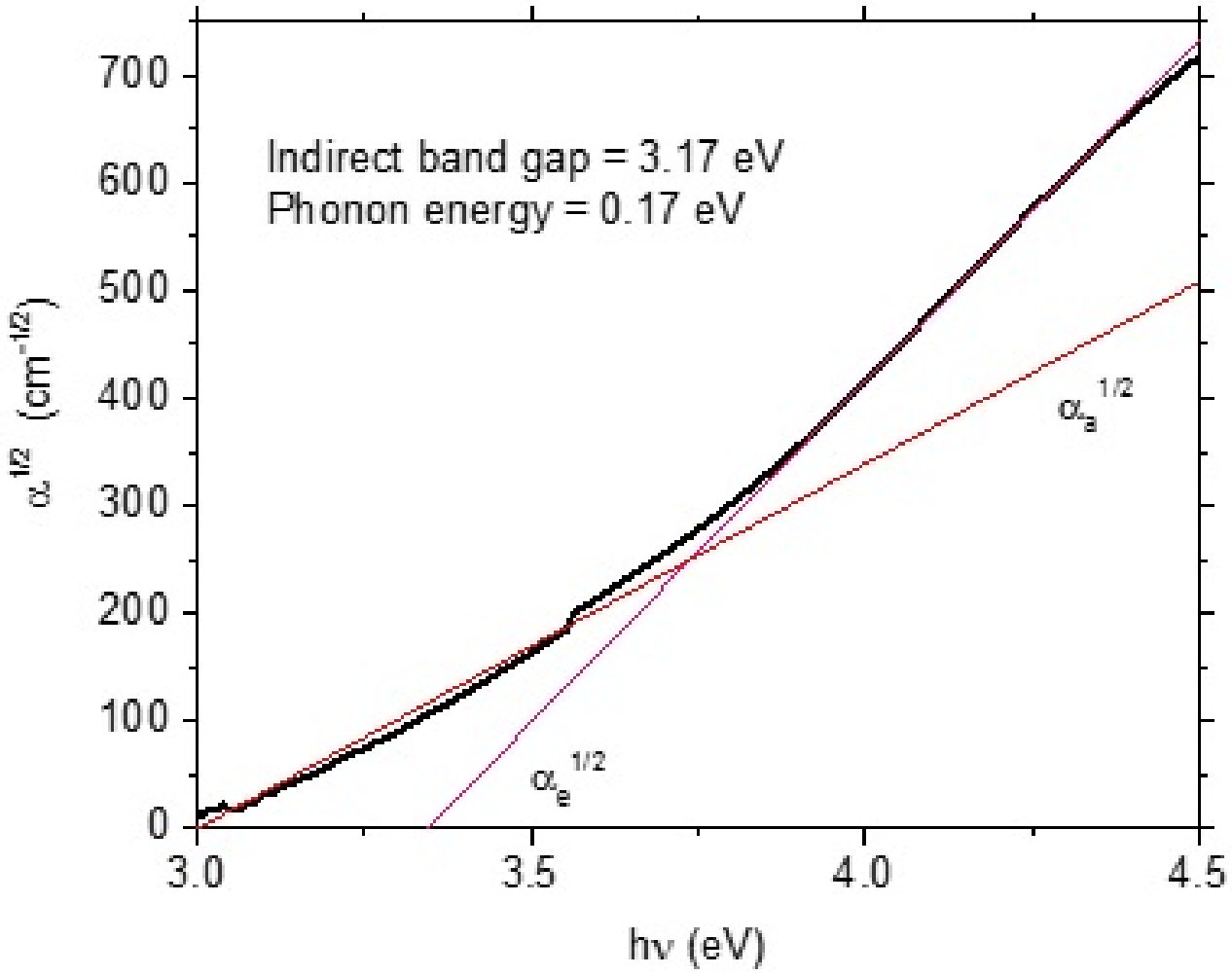

Figure 4.6: Determination of band gap of Smooth SPEED TiO_2 film.

$$\alpha_e + \alpha_a = C_e(T)(h\nu - E_g - E_p)^2 + C_a(T)(h\nu - E_g + E_p)^2, \tag{4.1}$$

where the coefficients depend on temperature-dependent phonon statistics. A plot of the square root of equation 4.1 gives a curve with two intersecting straight-line segments of different slope. The extension and intersection with the zero-absorption axis define the energies $E_g \pm E_p$. The determined values are given in figure 4.6. Often it is the experimental values of $\alpha h\nu$ that are equated to equation 4.1 [74]. A plot by this method analysis looks very similar to figure 4.6, but it gives the somewhat larger values E_g = 3.21 eV and E_p = 0.21 eV. The latter value is more within the range 3.2-3.35 eV reported for the indirect gap of Anatase [72, 75, 76, 77, 78, 79]. The phonon energy seems rather high, because the onset of optical phonon absorption appears below 0.1 eV, as shown figure 4.7. At high energies, the absorption coefficient increases less rapidly with photon energy.

Its functional dependence is expected to be $A(h\nu - E_g')^{\frac{1}{2}}$, where E_g' is the direct gap. We find E_g' to be about 4.2 eV by extrapolating a plot of to zero absorption. This value is higher than the expected value 3.8 eV [72]. However the portion of the spectrum that follows a square root function is very narrow, and it falls in a region of very low transmittance, so that the value of E_g' thus obtained has high uncertainty.

Figure 4.7 presents infrared spectra of the real and imaginary parts for the complex refractive index n + iκ , where n is the refractive index and κ is the extinction coefficient. These spectra compare well with previously published results for films deposited by Atomic Layer Deposition (ALD) [44] and sputtering[45] . For comparison we present our data for an evaporated film of the more common dielectric used in planer photonic devices SiO_2. In contrast with SiO_2, which has a strong and sharp extinction peak near 9 μm wavelength, the extinction of TiO_2 is relatively weak out to at least 11 μm wavelength. Thus, TiO_2 would be more attractive than SiO_2 as an index contrast material for Long-Wave Infrared LWIR photonic planer waveguides due to its comparatively low loss. Moreover, in contrast to the derivative-like feature in the refractive index of SiO_2, the index of TiO_2 changes monotonically.

This is particularly important in resonance absorption structures, such as metal-insulator-metal plasmonic absorbers, where derivative-like dispersion spectra give multiple absorption peaks that complicate the spectrum and interfere with spectral selectivity[48, 80].

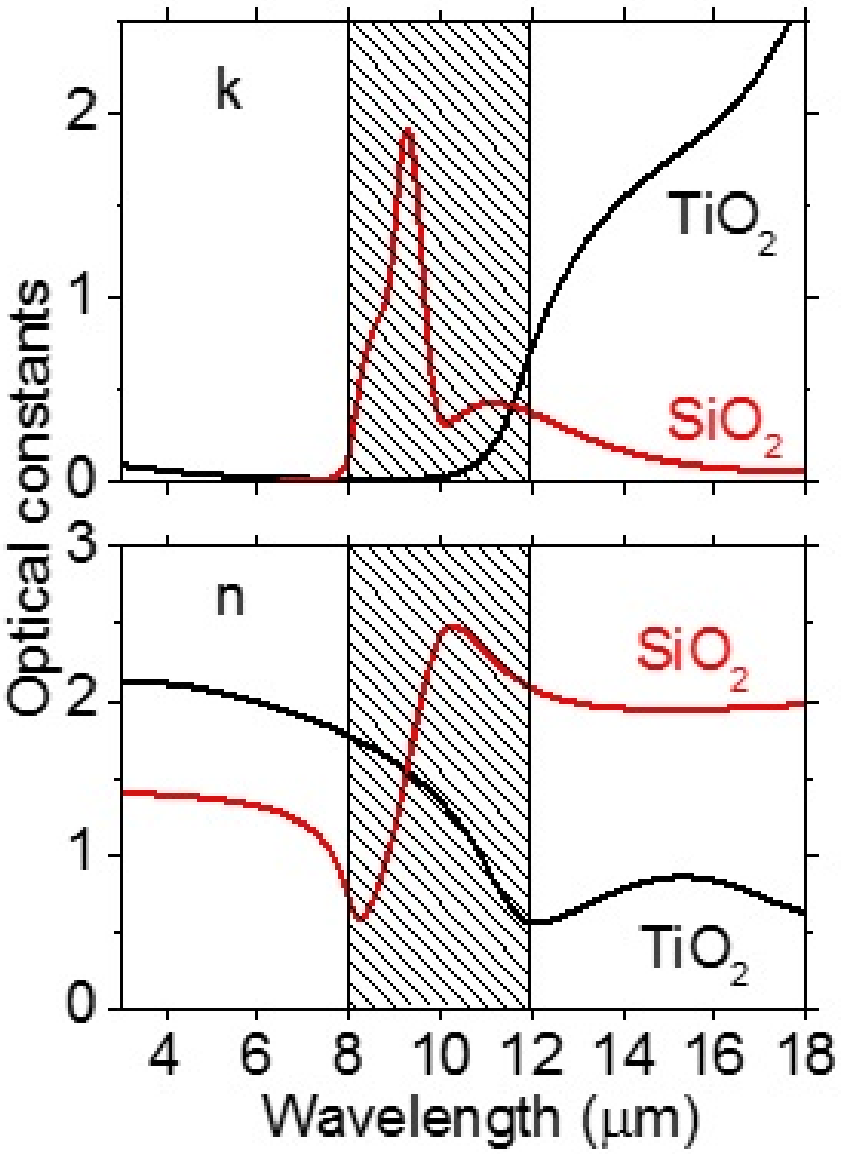

Figure 4.7: Infrared complex index spectra for Smooth SPEED TiO_2 and evaporated SiO_2 films. The shaded region indicates LWIR wavelengths.

The onset of extinction beyond 12 μm wavelength suggests optical phonon energies less than 0.1 eV. This is agreement with optical phonon frequencies determined from far-infrared reflectivity [81]. Thus, the phonon energy determined in from figure 4.6 is surprisingly large, unless fundamental absorption at the indirect gap is a two phonon process.

CHAPTER 5: RESULTS AND DISCUSSION OF EVAPORATED TiO_2

The XRD patterns were measured at a grazing incidence angle of 1° using CuKα radiation λ= 1.54059°A at 45 KV and 40 mA with a pattern recorded from 20° to 65° of 2θ. Evaporated TiO_2 is a Anatase phase, as shown in figure 5.1, after annealing. Before annealing, XRD had no sharp peaks, so as - evaporated film was amorphous.

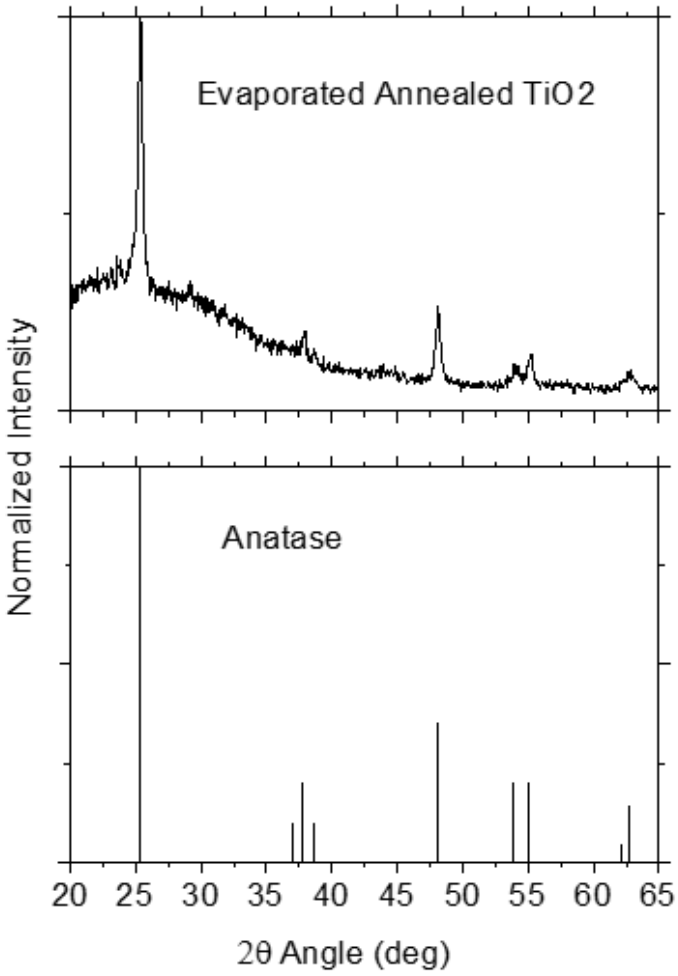

Figure 5.1: XRD measurement of Evaporated TiO_2 on Glass.

UV-visible transmittance measurements are analyzed to determine the band gap of each film. The absorption coefficient is related to the direct band gap and the incident photon energy by $\alpha h\nu = C(h\nu - Eg)^{\frac{1}{2}}$, Absorption coefficient was calculated according to Beers law, $\alpha = (\frac{1}{d}) \ln \frac{1}{T}$, Where d is film thickness. The band gap of evaporated TiO_2 is found to be about 4.0 eV, which appears some what high, though not as much so as for Smooth TiO_2 as shown in figure 5.2.

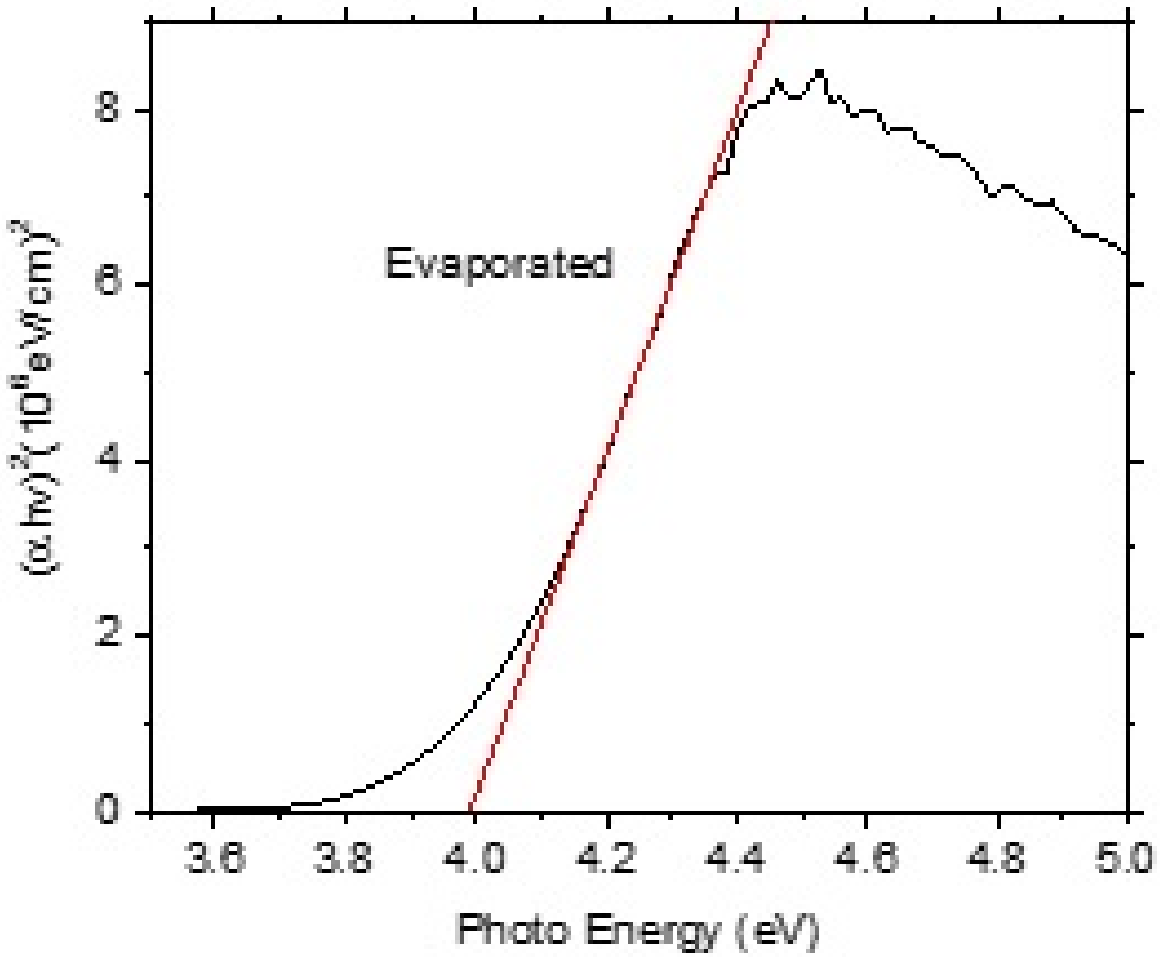

Figure 5.2: Band gap of E-beam evaporation.

The largest transmission of E-beam evaporation TiO_2 at 380 nm is 93% as figure 5.3. This film shows a complete Fabry- Perot oscillation. The separation in wave numbers $\Delta\tilde{\nu}$ is about 6700 cm^{-1}. The separation should equal $\frac{1}{(2nd)}$, which for n= 3 is 7200 cm^{-1}. The observed value is smaller because fundamental absorption crops the short wave peak.

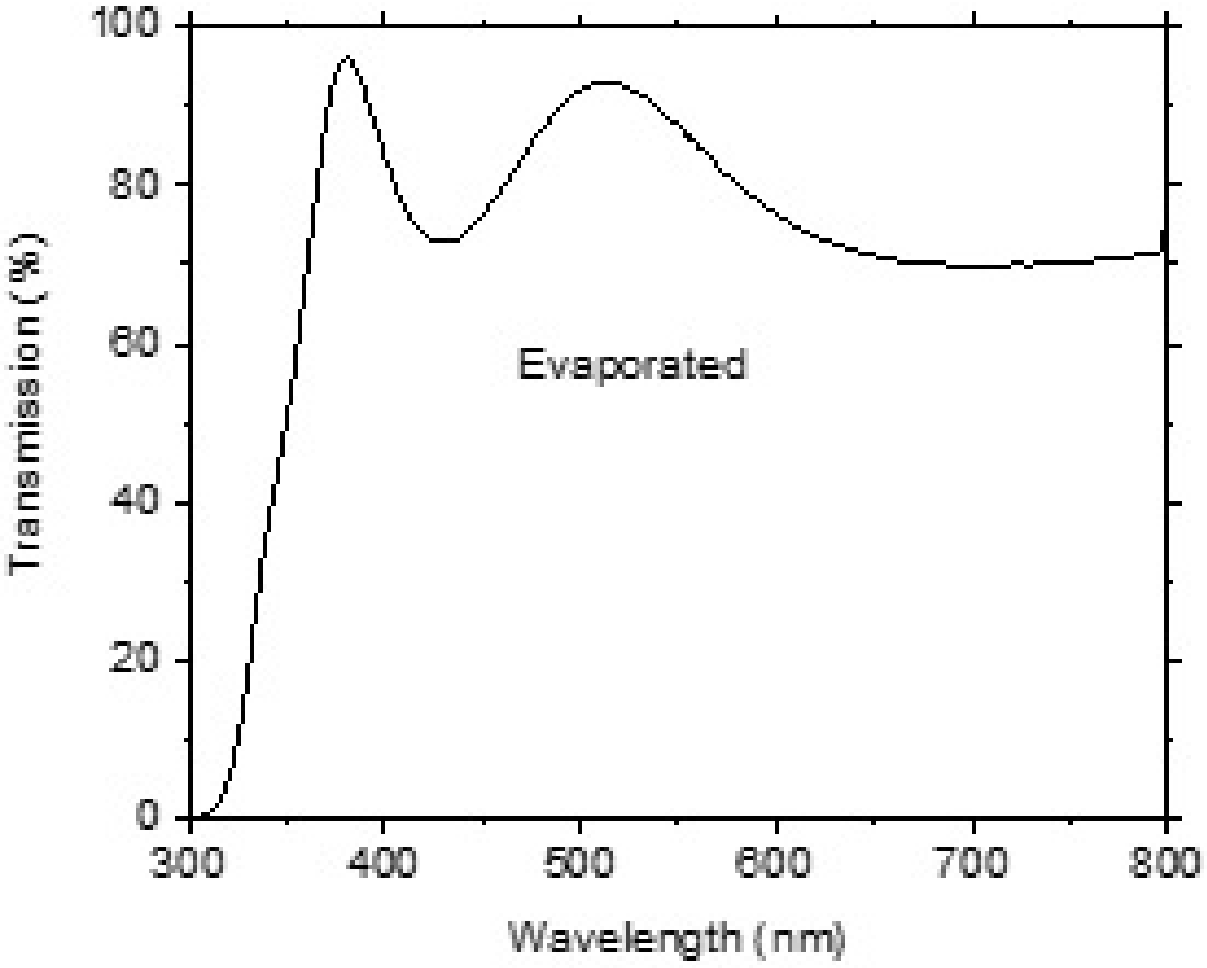

Figure 5.3: Transmission of E-beam evaporation .

Evaporated TiO_2 is rough with large surface area as shown in figure 5.4

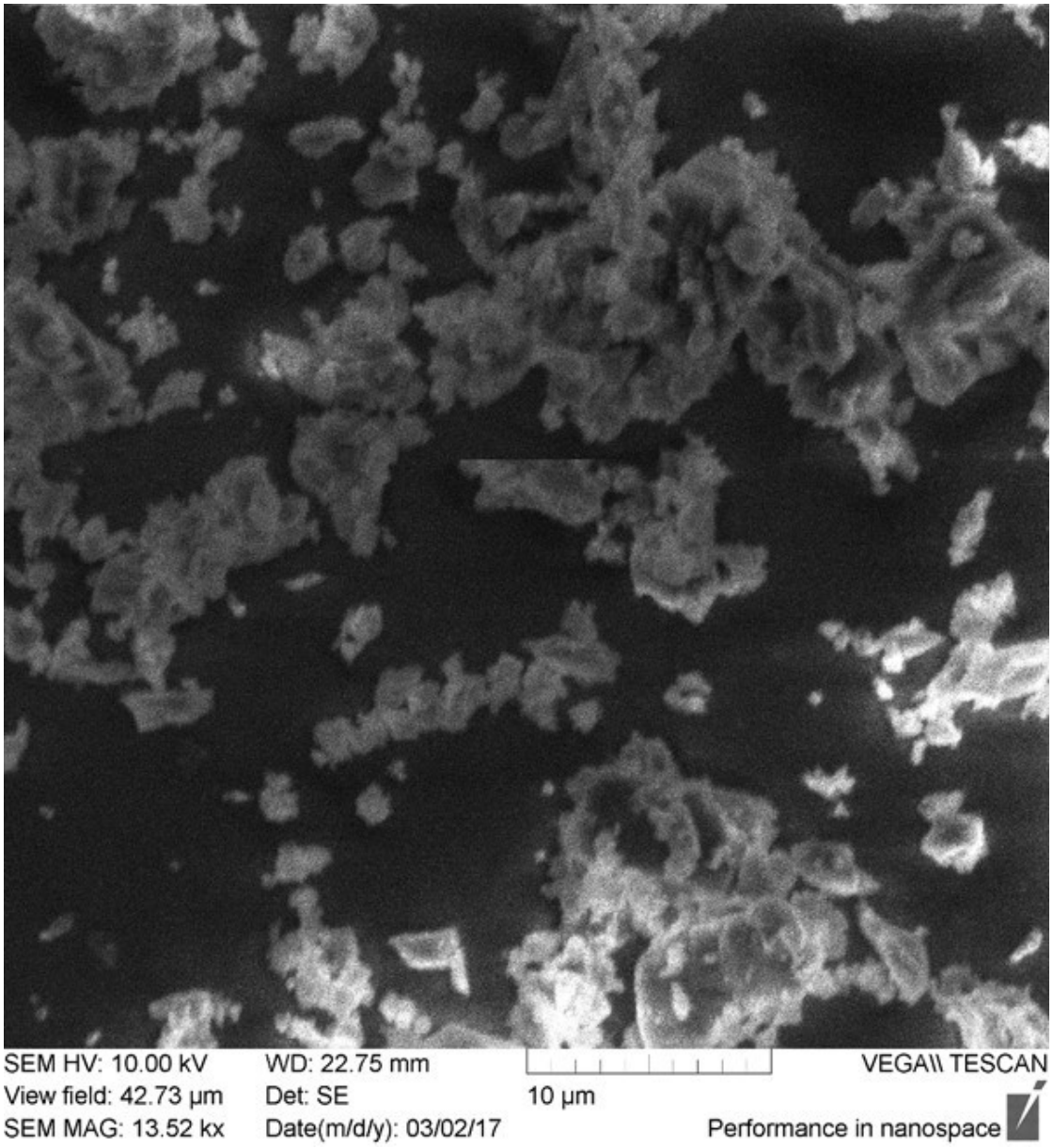

Figure 5.4: SEM Top View of Evaporated TiO_2.

SEM cross-section of Evaporated TiO_2 has thickness $\sim$ 230 nm as shown in figure 5.5

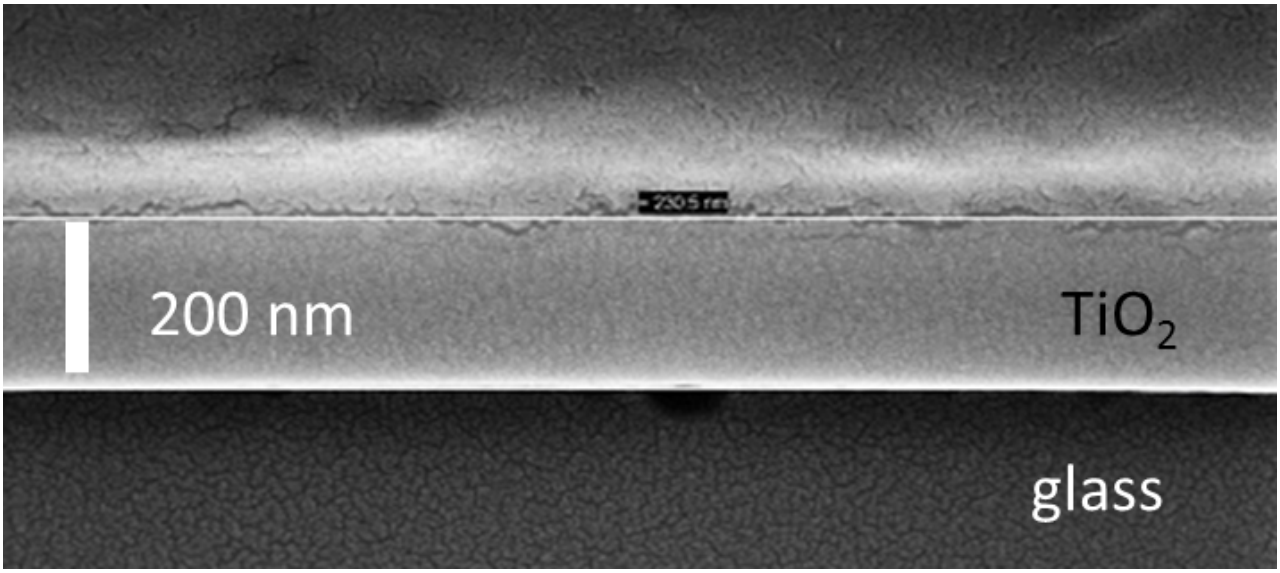

Figure 5.5: SEM cross-sectional image of Evaporated TiO_2 film.

Atomic Force microscopy (AFM) images of the TiO_2 films obtained using (DI) Digital Instruments 5000U, which operated in the constant mode by putting a sample under Silicon with Aluminum reflex coating tip, scanning in Air. The spring constant of the Cantilever was 40 N/m and resonant frequency was 300 kHz. Actual resonant frequency was 280.69 kHz and actual spring constant was 31.01 N/m. Scan size was 30μ m. AFM analyzed of all samples (Ropy, Smooth, and Evaporated). By using (DI) Digital Instruments 5000U. Data visualization and analysis used to Gwyddion program.

An AFM image for the evaporated sample is presented in figure 5.6. It shows the surface comprises flat terraces with a small number of defects. Scan area of AFM image 30 μm x-axes, 15 μm y-axes. The vertical dimension range is 0.13 μm.

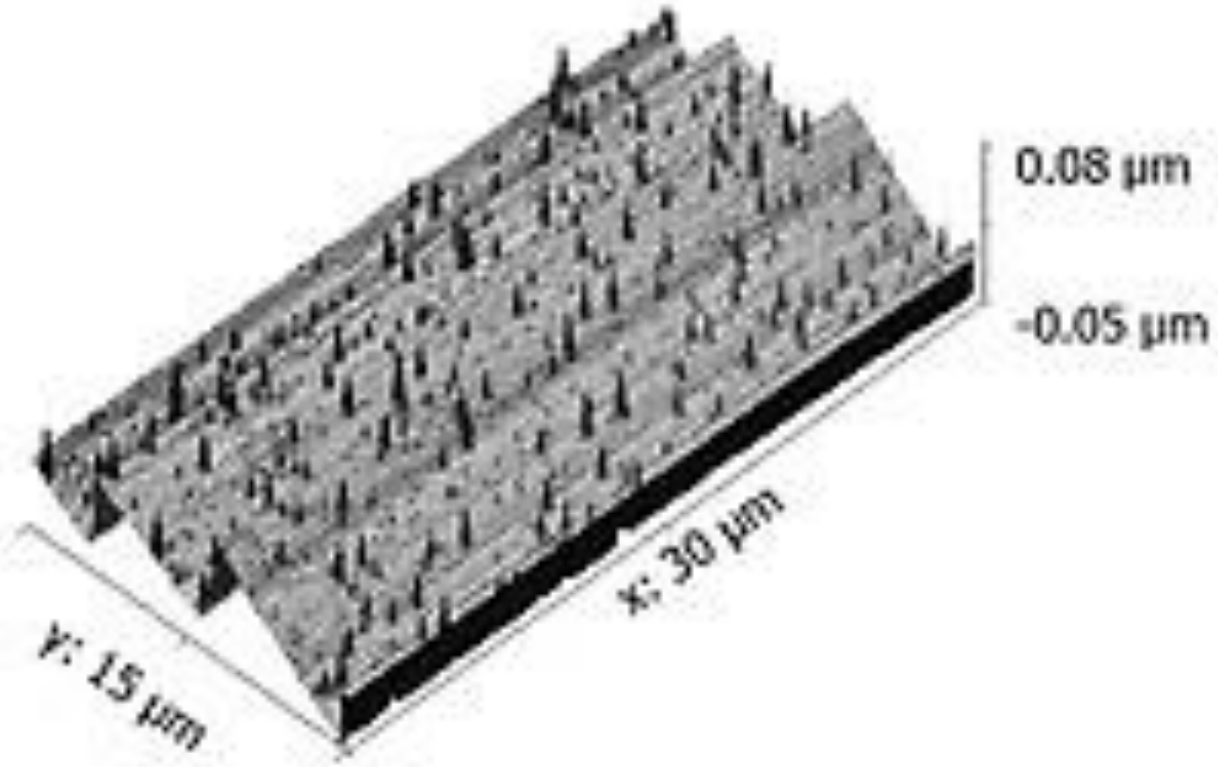

Figure 5.6: AFM 3-Dimensions of Evaporated TiO_2 Sample.

CHAPTER 6: RESULTS AND DISCUSSION OF SPEED $BaTiO_3$ FOR PYROELECTRICS

Figure 6.1-a presents a top-view SEM image of a $BaTiO_3$ film grown by SPEED. The film comprises a sea of nano crystals, in which are embedded micron-sized single-crystal islands. Figure 6.1-b presents a cross sectional SEM image of the film, revealing a 2 μm film thickness.

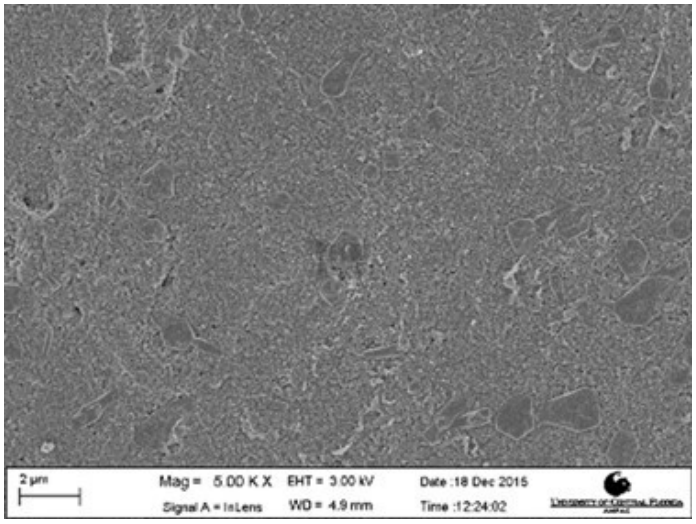

(a)

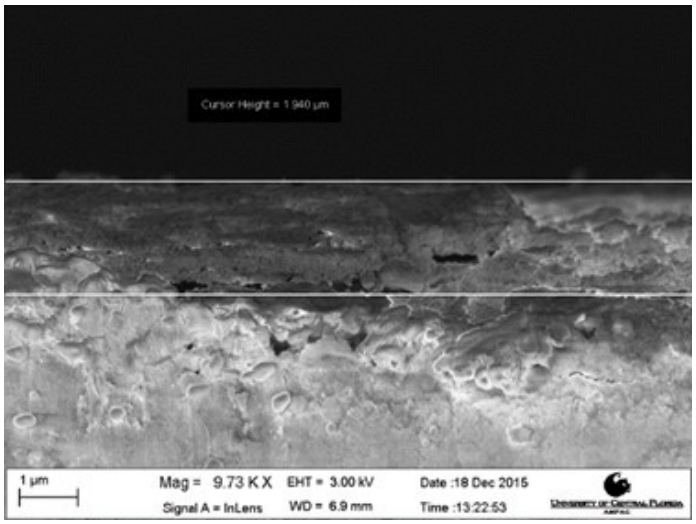

(b)

Figure 6.1: SEM images of SPEED-grown $BaTiO_3$ films. Figure 6.1-a is a top view revealing a mix of nano- and micro-meter scale crystals. Figure 6.1-b is a SEM cross section.

Figure 6.2 presents XRD spectra for two different annealing temperatures indicated.

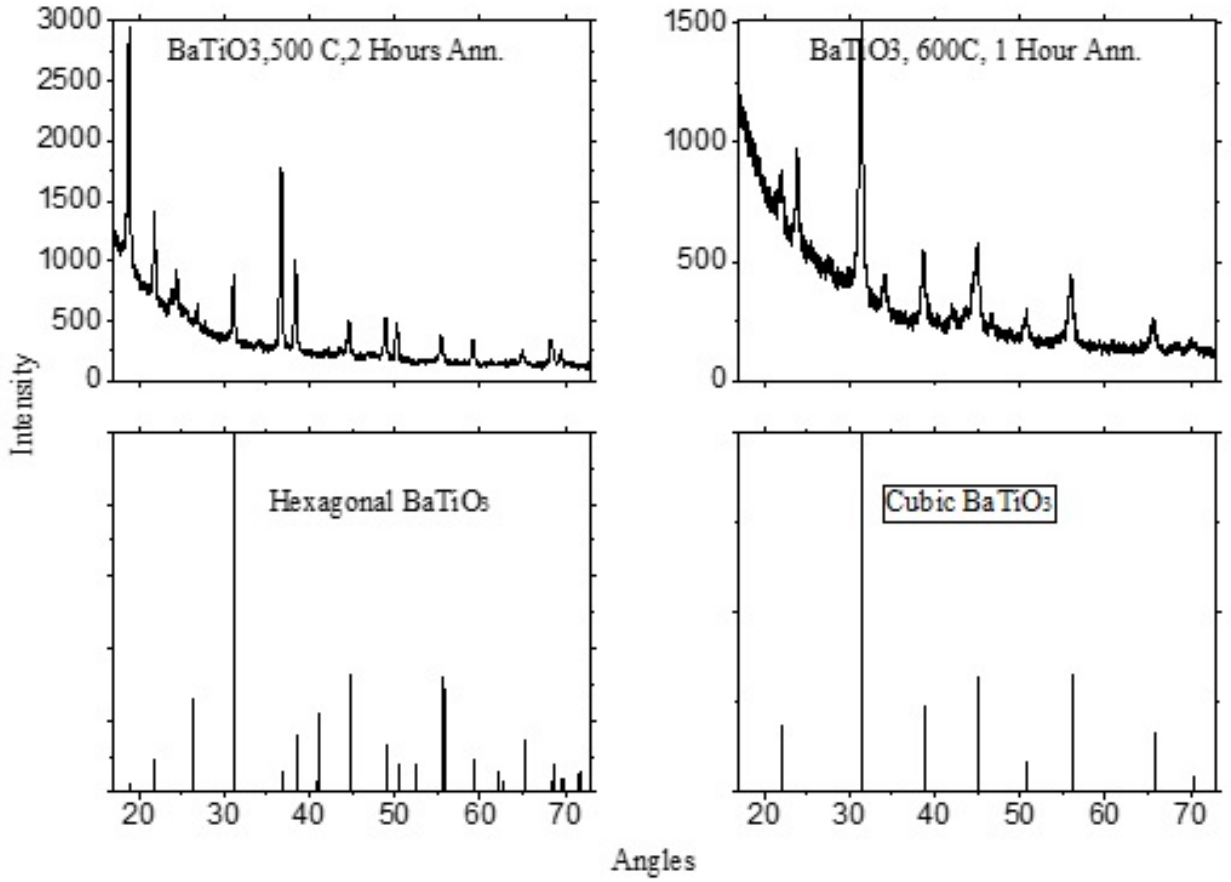

Figure 6.2: XRD spectra of SPEED-grown $BaTiO_3$ thin films.(left) $BaTiO_3$, $500°C$, 2 hours annealed. (right) $BaTiO_3$, $600°C$, 1 hour annealed.

Reference spectra are also presented, showing that the sample annealed at $500°C$, 2 hours is hexagonal, while the sample annealed at $600°C$, 1 hour has converted to the non-pyroelectric cubic phase. Notable differences are that the latter is missing the peaks evident in the spectrum of the former near 18, 37, 49, 59, and 69 degrees. Both measured spectra contain peaks that are absent from either reference spectrum. Extra peaks at 24, 34 and 42.5 deg are stronger in the $600°C$ annealed sample, which also contains an extra line at 46 deg absent for the $500°C$ sample. These extra peaks suggest the presence of one of the other $BaTiO_3$ phases that tends to increase on annealing at $600°C$.

Figure 6.3-a presents an oscilloscope screen shot with a response transient for a sample annealed at $500°C$ for 2 hours. The decay time is about 5 ms. There is strong electrical disturbance due to the laser pulsing circuit at times earlier than shown, with the result that when the laser beam is shuttered, there is a negative signal of about the same magnitude in the region indicated by the boxcar gate (channel 2).

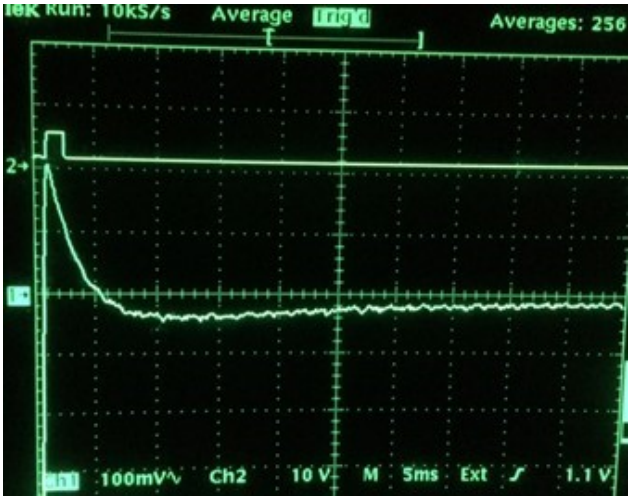

(a)

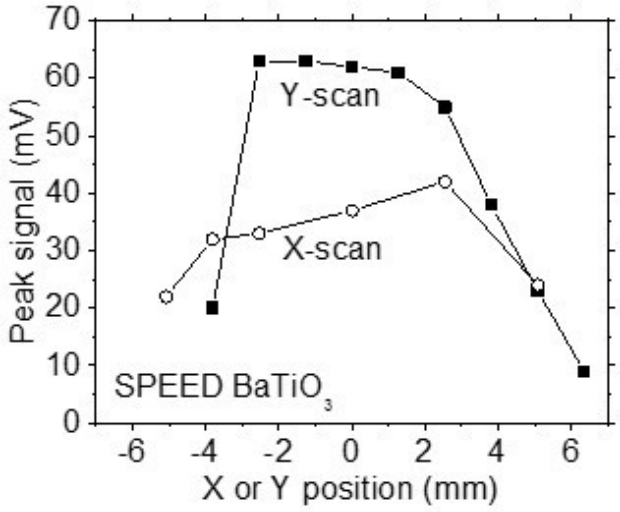

(b)

Figure 6.3: Figure 6.3-a is an oscilloscope screen shot showing the transient pyroelectric response to the laser pulse on channel 1. Channel 2 shows the gate of a boxcar average. Figure 6.3-b is a peak signal as function of position on the absorbing area of the $BaTiO_3$ device.

Thus, the peak photo response is about 400 mV, or 8 V/J for the sample and amplifier combination. This signal was 10x stronger than for a similar sample annealed half as long (1 hr at $500°$C). Figure 6.3-b presents a measurement of photo-response as a function of position on the 1 cm^2 area of the carbon-black coating.

The sample was translated using an x-y stage. The point (0, 0) corresponds to the center of the sample. The x-scan was performed at y = zero and vice versa. The photo response appears to be fairly uniform across the active area, dropping steeply the edges of the carbon-black square.

Note that the signal strength in figure 6.3-a is smaller than in figure 6.3-b which was measured about one week earlier. The photo-response was found to decay over time, presumably due to the absorption of water vapor from the air.

Figure 6.4-a presents a plot of 4 measurement points collected over a period of 3 weeks. The decay has a characteristic time of 1 week. Baking at 100°C restores the response, as shown in figure 6.4-b.

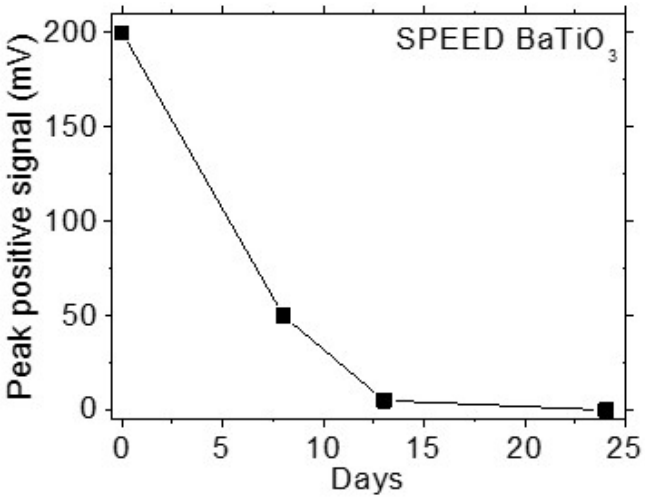

(a)

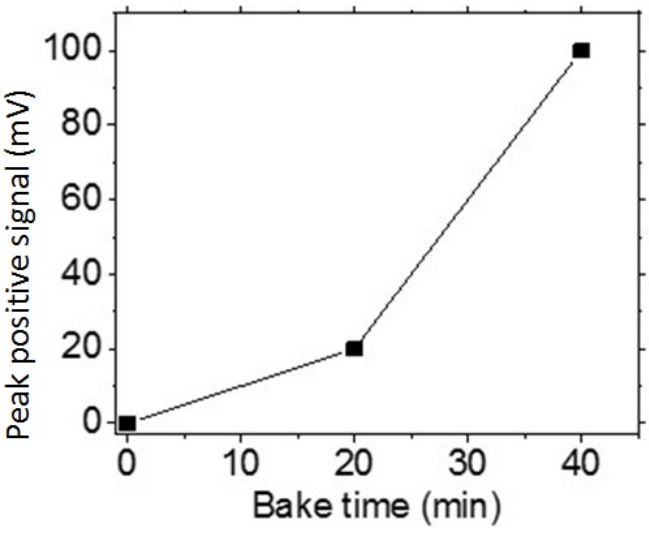

(b)

Figure 6.4: Figure 6.4-a is decay in peak photo-response with time for sample kept in air. Figure 6.4-b is a recovery of signal on baking at 100°C.

Poling experiments were performed on the sample on day 13 as shown in figure 6.4, when the signal had decayed almost to zero. This was achieved by applying a DC voltage between top and substrate surfaces of the sample with the op-amp power turned off. Voltages of 0.5 and 1 V applied for 2 minutes produced no effect. Voltages of 2 V applied for 2 minutes produced a negative signal with -40 mV peak amplitude, and this signal had the opposite sign from the original signal of the unpoled sample. The signal achieved by poling decayed in ~ 1 min. The sample could be poled again, and the behavior was repeatable. When poling of the opposite sign was applied, the photoresponse was positive.

Figure 6.5 presents a high resolution top-view SEM image of another $BaTiO_3$ film. We refer to this film as $BaTiO_3$ even though subsequent analysis shows that it is only partially composed of this compound, in contrast to our previously reported films [69], in which $BaTiO_3$ was the dominant crystalline phase. The SEM image reveals grains with a size distribution of about 50 to 200 nm. Additional SEM images reveal a fine grained matrix that contains cracks.

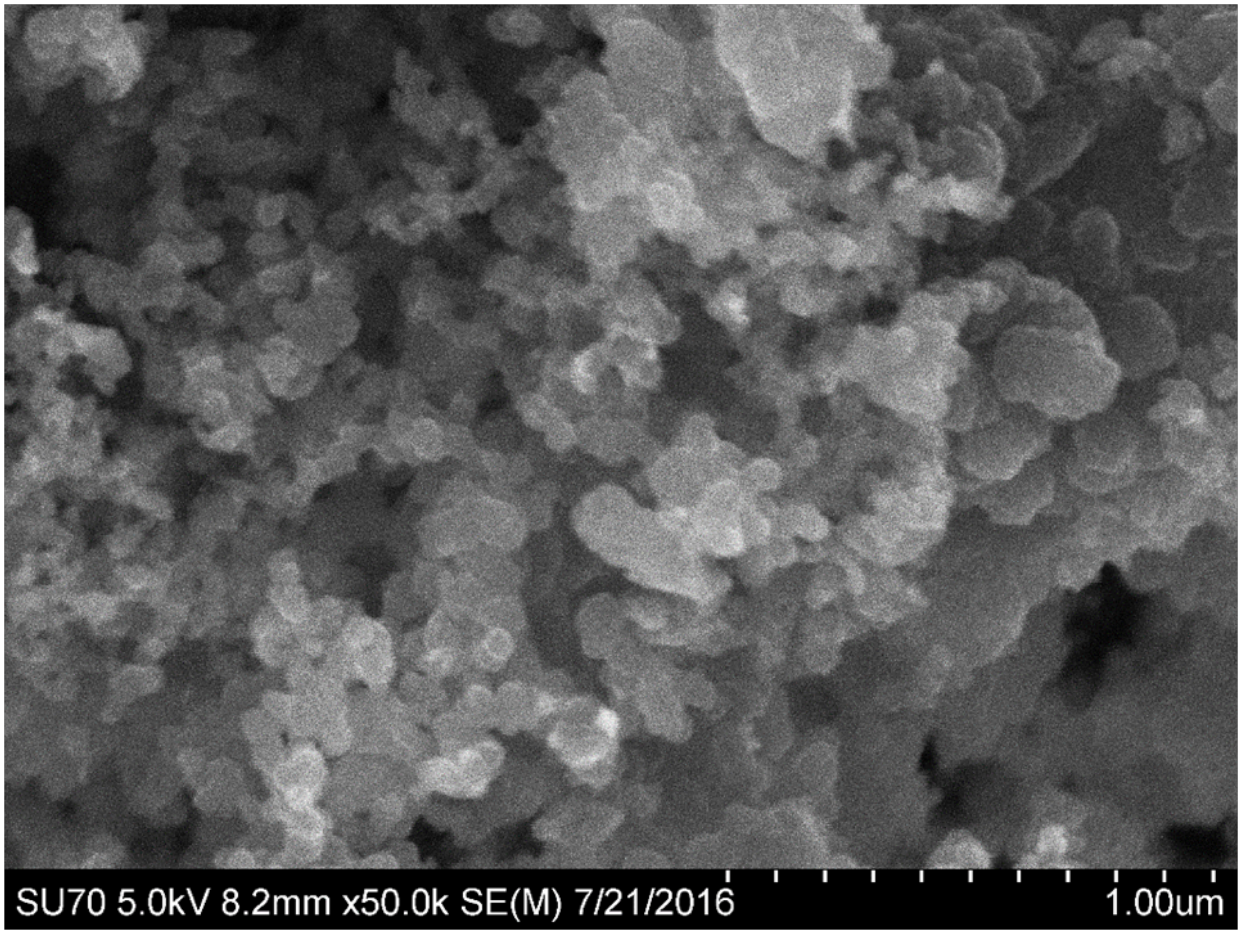

Figure 6.5: High resolution SEM image of SPEED-grown $BaTiO_3$ thin film.

Figure 6.6 presents an SEM image of the surface at the edge of the carbon-black coating at low magnification. The $BaTiO_3$ film has a white crust, which EDX shows to be up to 35% Cl. This indicates that the Cl byproduct was incompletely volatized, and it suggests the need for longer and hotter anneals. EDX on the carbon-black film shows almost exclusively carbon. Cross sectional SEM imaging shows the $BaTiO_3$ and C-black films to be $\sim$1 and $\sim$30 μm thick, respectively.

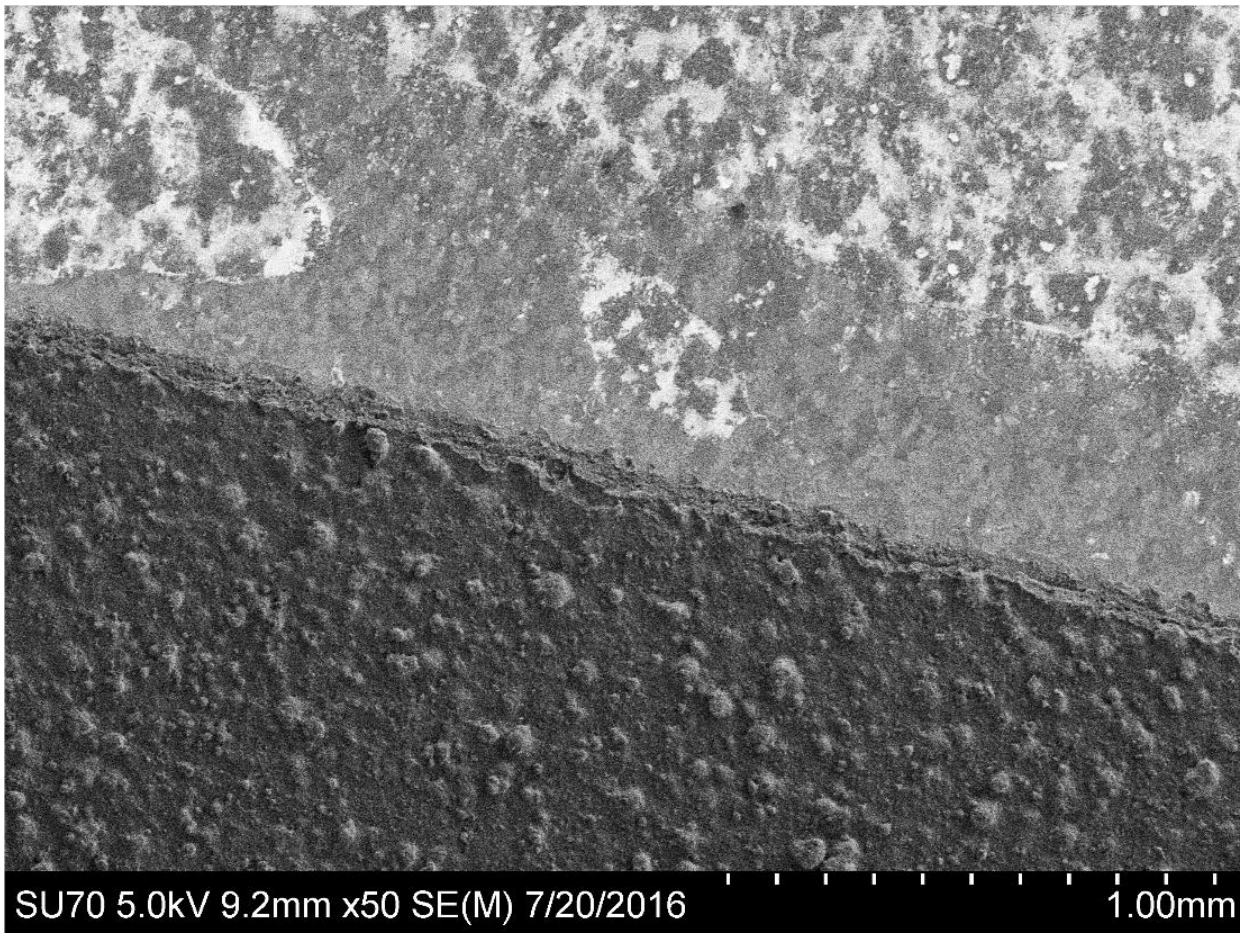

Figure 6.6: SEM image of surface of SPEED-grown $BaTiO_3$ film with carbon-black coating (lower region).

Figure 6.7 presents powder XRD reference data for the various phases of $BaTiO_3$.

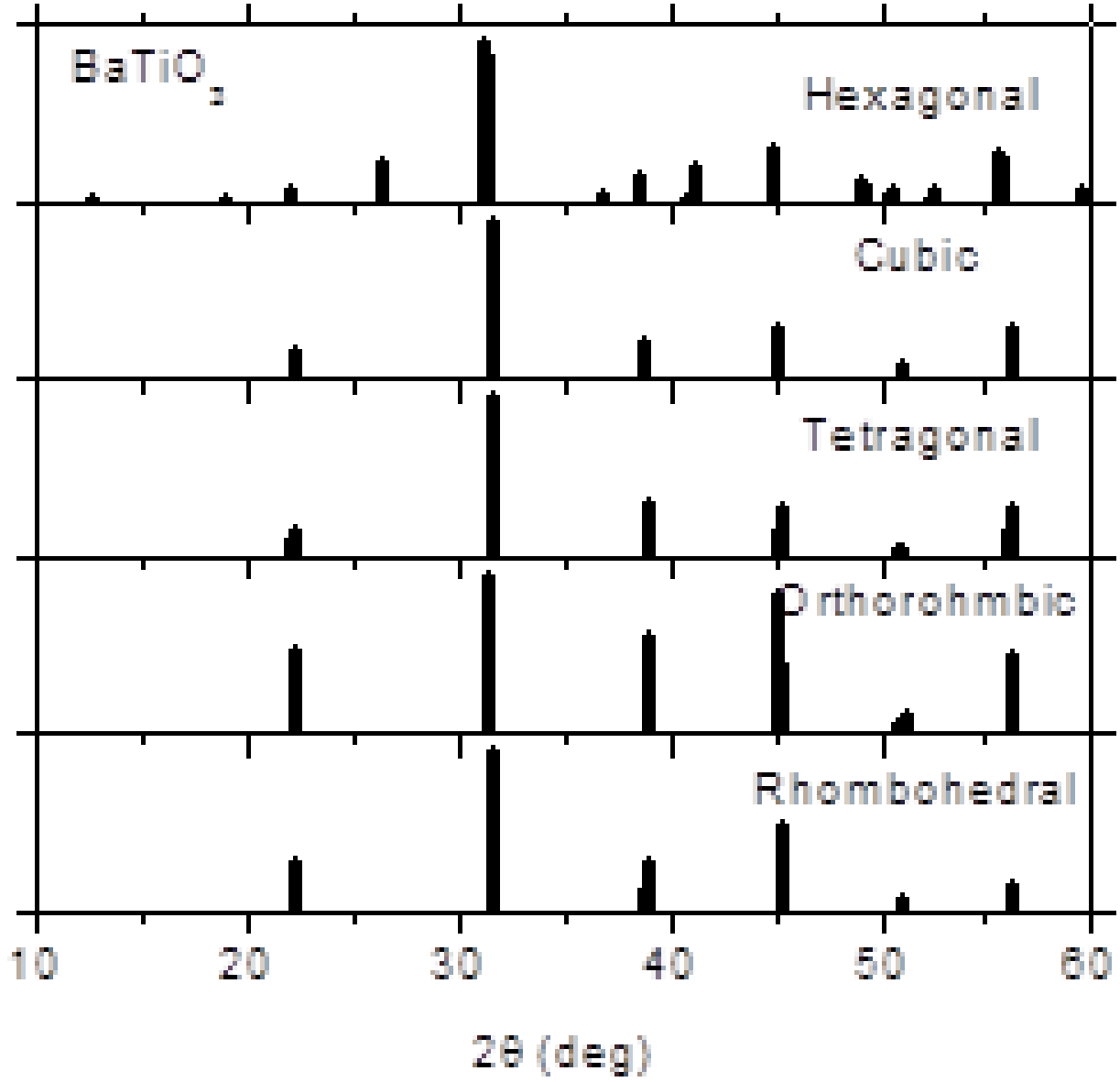

Figure 6.7: Reference Powder XRD spectra for the five phases of $BaTiO_3$.

The signal-to-noise ratio is sufficiently low in the XRD data for our thin films that the non-hexagonal phases would be difficult to distinguish from each other. The XRD pattern for the hexagonal phase is much different than the others.

The relative intensities of XRD peaks for nano-crystalline thin films can differ significantly from those of the powder due to interactions with the substrate.

Figure 6.8 compares our measured XRD data for films annealed after growth at the three different temperatures 450, 500, and 600°C.

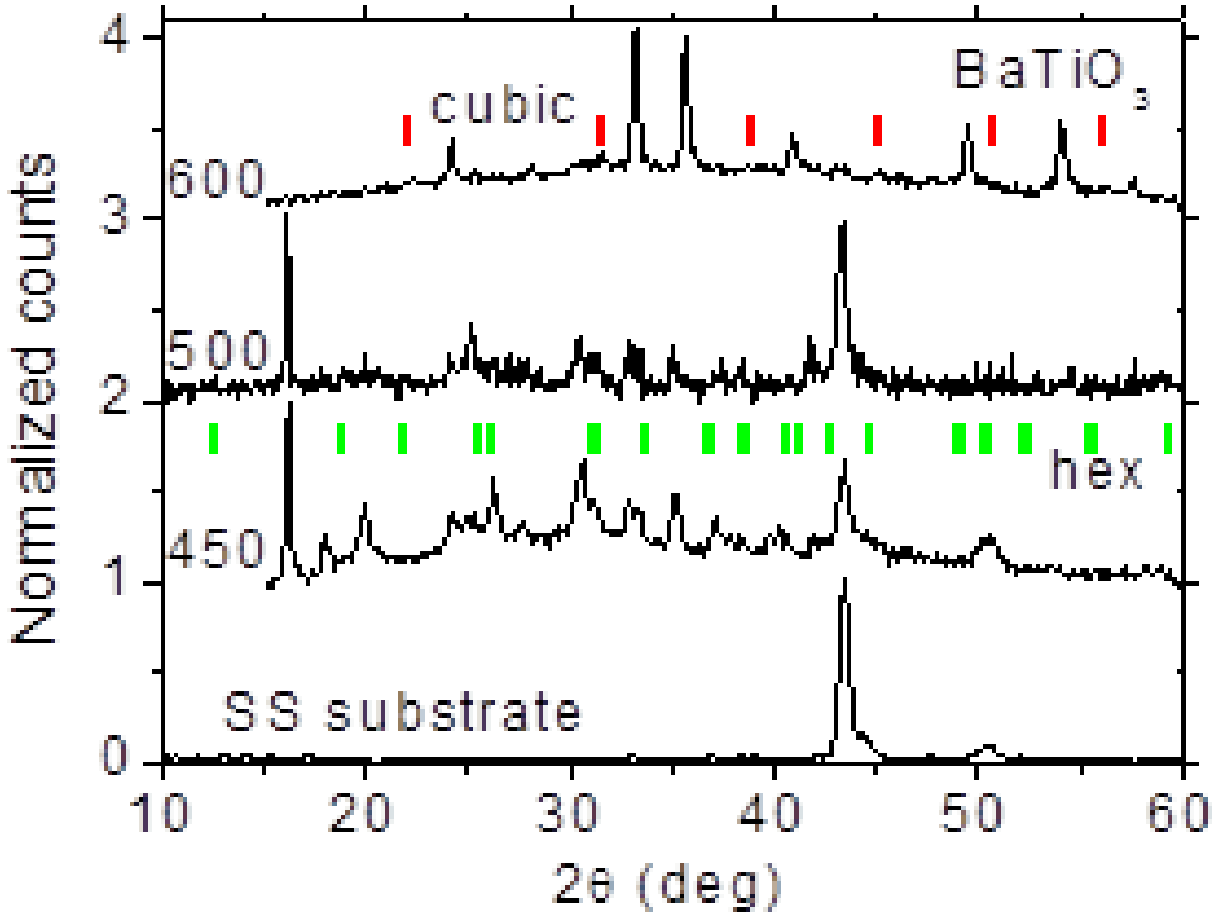

Figure 6.8: XRD spectra of SPEED-grown $BaTiO_3$ thin films. Annealing temperatures in degrees C and the reference positions of XRD peaks for cubic and hexagonal phases are indicated.

The annealing times were one, 2, and 4 hours respectively. At a given annealing temperature, the XRD spectrum was independent of annealing time in the range 1-4 hours. The substrate spectrum was taken on the backside of the substrate and reveals substrate lines at $\sim$ 44 and 51 degrees. These substrate lines appear as artifacts in the XRD of the two lower-temperature annealed samples. The expected peak positions for hexagonal and cubic $BaTiO_3$ are indicated. In all three spectra, the dominant peaks do not belong to any of the 5 $BaTiO_3$ phases.

In the two lower temperature annealed samples there are several weak peaks that could correspond to the hexagonal phase, but they could with equal probability be assigned to phases of residue $TiCl_2$, $TiCl_3$, or $TiCl_4$, and the strongest peaks in these spectra belong with high confidence to a hexagonal phase of $TiCl_3$, which itself could be pyroelectric. In the $600°$C annealed sample there are a few small XRD peaks that can be identified with one of the non-hexagonal phases. Thus it appears that the films are a mixture of $BaTiO_3$ nano-crystals in a matrix of some other polycrystalline material.

The transition from hexagonal to one of the other phases with increasing annealing temperature agrees with our previous observation on a different set of $BaTiO_3$ films [69], which were more nearly pure $BaTiO_3$. Scherrers formula [82] indicates that the lower bound on the mean size of the ordered crystalline domains of $BaTiO_3$ is $\sim$ 20 nm.

Figure 6.9-a presents photoresponse data for a carbon-black coated sample annealed at 500° C for 2 hours using measurement system A.

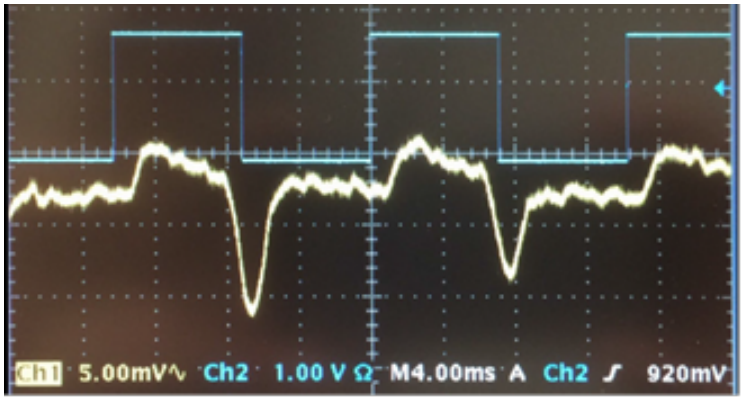

(a)

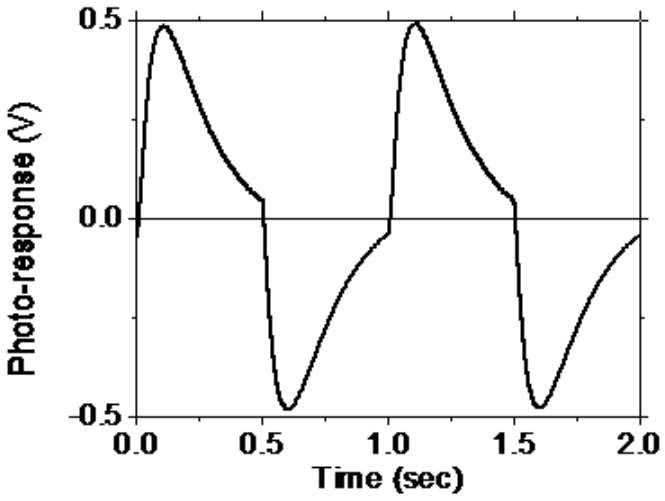

(b)

Figure 6.9: Figure 6.9-a is an oscilloscope screen shot showing pyroelectric response to 100 mW CO_2 laser chopped at 70 Hz, amplifier A. Figure 6.9-b is a response to 13 mW/cm^2 broad-band IR source chopped at 1 Hz, amplifier B.

The signal comprises a peak when the chopped laser first illuminates the sample, and a smaller and slower signal when the laser is chopped off. The response time is about 1 ms. The responsivity is about 100 mV/W, compared with the $\sim$1 μV/W we previously reported for a more-nearly pure hexagonal $BaTiO_3$ film using a 100 ns pulsed CO_2 TEA laser with a similar amplifier [69]. That earlier peak response was reduced by the ratio of laser pulse duration to system response time, $100ns/5ms = 20 \times 10^{-6}$. Scaling the earlier result by that ratio gives $\sim$50 mV/W as the probable response that would be measured for that earlier film using measurement system A. Thus, the present measurement is in agreement with the earlier one.

Figure 6.9-b presents photo-response using measurement system B. The signal is now symmetric with respect to the on-off chopping of the source. The peak output voltage was 0.5 V. The response has a 400 ms time constant, which is slower than expected for the 7.2 Hz filter cut-off frequency. With system B, we achieve responsivity of 40 V/W.

Previously we reported the appearance of a short-lived (1 min) photoresponse that appeared after poling the film with a few volts bias at room temperature. The sign of the photoresponse depended on the sign of the applied bias. We now interpret this effect as poling-induced charging of traps, whose spatial distribution depends on the sign of the applied bias. When the sample is hit by infrared, these traps are thermally discharged, giving a current that is comparable to pyroelectric current. As soon as the traps are all emptied, the effect disappears. This effect is known to be especially significant in thin films. [83]

Figure 6.10 presents ferroelectric hysteresis measured on the film studied in ref.[69], which is 5x smaller than the value for bulk $BaTiO_3$ [84]. That film was primarily hexagonal phase, with significant admixture of some other material, which can explain the relative smallness of its polarization compared to bulk tetragonal $BaTiO_3$.

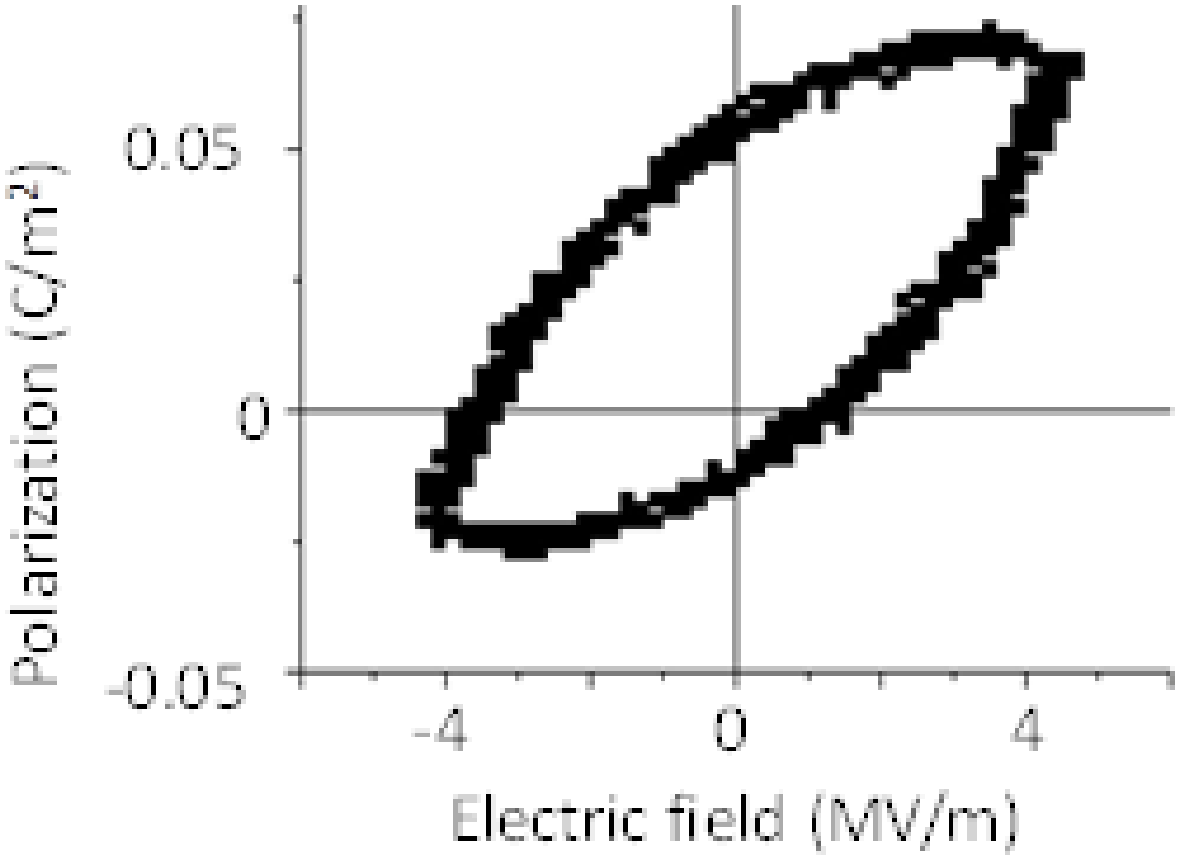

Figure 6.10: Ferroelectric hysteresis curve of $BaTiO_3$ thin film.

Refs.[49], and [66] described a design for spectrometer on a chip. The design comprised a broadband IR source, rectangular photonic waveguide, interaction region, dispersion region, and detectors.

In that work, only the waveguide section formed by deep reactive ion etching of silicon had actually been fabricated. The proposed sources were IR LEDs, but integrating these onto the chip had not been considered. An adiabatic taper transduced the photons in the waveguide to surface plasmons polaritons that existed in a gap between the outer side walls of the narrowed waveguide and vertical side walls of border material coated with suitable conductor. We have since demonstrated perfectly conformal conducting SnO_2:F that can be deposited by SPEED on such sidewalls to support surface plasmons in this interaction region [68]. With Ref.[69] and this paper we have presented first results on a pyroelectric $BaTiO_3$ detector material, which can be deposited by SPEED, and which in principle can be positioned at the end of a waveguide by standard photolithographic patterning. Clearly, considerable work remains to optimize the film, to develop processes and to design suitable amplifiers.

CHAPTER 7: CONCLUSION AND FUTURE WORKS

We reported physical, electrical, and optical properties of nano-crystalline orthorhombic Ropy TiO_2 thin films of micron thickness grown by an aqueous spray deposition method. The proposed Perovskite Solar Cell presented is a type of considerable current interest, which can benefit from our TiO_2 layer as electron collector, and which can be entirely fabricated by our aqueous process. Work to complete and test such a cell is ongoing.

We presented optical and morphological properties of Smooth TiO_2 film grown by aqueous spray deposition. The crystalline phase is Anatase. Defects that are present are much smaller than long-wave infrared wavelengths (LWIR) and should not contribute significantly to electrodynamic losses. Low dispersion in the long-wave infrared is attractive for plasmonic resonant absorbers in applications that require spectral selectivity.

$BaTiO_3$ thin films were grown by an aqueous spray deposition process at moderate substrate temperatures. Two phases were observed depending on annealing temperature. The hexagonal phase demonstrated a pyroelectric infrared photoresponse. An aqueous spray deposition process grew $BaTiO_3$ thin films. Two phases were observed, depending on annealing temperature, in a matrix of some other material.

LIST OF REFERENCES

[1] Henry J Snaith. Perovskites: the emergence of a new era for low-cost, high-efficiency solar cells. *The Journal of Physical Chemistry Letters*, 4(21):3623–3630, 2013.

[2] Martin A Green, Keith Emery, Yoshihiro Hishikawa, Wilhelm Warta, and Ewan D Dunlop. Solar cell efficiency tables (version 45). *Progress in photovoltaics: research and applications*, 23(1):1–9, 2015.

[3] National Renewable Energy Laboratory (NREL). `http://www.nrel.gov/ncpv/`, 2016.

[4] Shuangyong Sun, Teddy Salim, Nripan Mathews, Martial Duchamp, Chris Boothroyd, Guichuan Xing, Tze Chien Sum, and Yeng Ming Lam. The origin of high efficiency in low-temperature solution-processable bilayer organometal halide hybrid solar cells. *Energy & Environmental Science*, 7(1):399–407, 2014.

[5] Christian Wehrenfennig, Mingzhen Liu, Henry J Snaith, Michael B Johnston, and Laura M Herz. Homogeneous emission line broadening in the organo lead halide perovskite ch3nh3pbi3–x cl x. *The journal of physical chemistry letters*, 5(8):1300–1306, 2014.

[6] Guichuan Xing, Nripan Mathews, Shuangyong Sun, Swee Sien Lim, Yeng Ming Lam, Michael Grätzel, Subodh Mhaisalkar, and Tze Chien Sum. Long-range balanced electron- and hole-transport lengths in organic-inorganic ch3nh3pbi3. *Science*, 342(6156):344–347, 2013.

[7] Gill Sang Han, Young Hyun Song, Young Un Jin, Jin-Wook Lee, Nam-Gyu Park, Bong Kyun Kang, Jung-Kun Lee, In Sun Cho, Dae Ho Yoon, and Hyun Suk Jung. Reduced graphene oxide/mesoporous tio2 nanocomposite based perovskite solar cells. *ACS applied materials & interfaces*, 7(42):23521–23526, 2015.

[8] Sunil H Chaki, MP Deshpande, and Jiten P Tailor. Characterization of cus nanocrystalline thin films synthesized by chemical bath deposition and dip coating techniques. *Thin Solid Films*, 550:291–297, 2014.

[9] Dinesh K Patel, Alexander Kamyshny, Huang Zhen, Shlomo Magdassi, et al. Fabrication of transparent conducting films composed of in 3+ doped cus and their application in flexible electroluminescent devices. *Journal of Materials Chemistry C*, 3(33):8700–8705, 2015.

[10] Sarmad Fawzi Hamza Alhasan, Farnood Khalilzadeh-Rezaie, Robert E Peale, and Isaiah O Oladeji. Ropy foam-like tio 2 film grown by water-based process for electron-conduction layer of perovskite solar cells. *MRS Advances*, 1(46):3169–3174, 2016.

[11] Teddy Salim, Shuangyong Sun, Yuichiro Abe, Anurag Krishna, Andrew C Grimsdale, and Yeng Ming Lam. Perovskite-based solar cells: impact of morphology and device architecture on device performance. *Journal of Materials Chemistry A*, 3(17):8943–8969, 2015.

[12] Atsushi Kogo, Masashi Ikegami, and Tsutomu Miyasaka. A sno x–brookite tio 2 bilayer electron collector for hysteresis-less high efficiency plastic perovskite solar cells fabricated at low process temperature. *Chemical Communications*, 52(52):8119–8122, 2016.

[13] Jacob Tse-Wei Wang, James M Ball, Eva M Barea, Antonio Abate, Jack A Alexander-Webber, Jian Huang, Michael Saliba, Iván Mora-Sero, Juan Bisquert, Henry J Snaith, et al. Low-temperature processed electron collection layers of graphene/tio2 nanocomposites in thin film perovskite solar cells. *Nano letters*, 14(2):724–730, 2013.

[14] M Kawachi, M Yasu, and T Edahiro. Fabrication of sio2-tio2 glass planar optical waveguides by flame hydrolysis deposition. *Electronics letters*, 19(15):583–584, 1983.

[15] David G Cahill and Thomas H Allen. Thermal conductivity of sputtered and evaporated sio2 and tio2 optical coatings. *Applied Physics Letters*, 65(3):309–311, 1994.

[16] Hiroyuki Nasu, Kiyoshi Kurachi, Akihiro Mito, Hideki Okamoto, Jun Matsuoka, and Kanichi Kamiya. Second harmonic generation from an electrically polarized tio2-containing silicate glass. *Journal of non-crystalline solids*, 181(1-2):83–86, 1995.

[17] Kie Y Ahn and Leonard Forbes. Capacitor structure forming methods, September 7 2004. US Patent 6,787,413.

[18] AI Abdulagatov, Y Yan, JR Cooper, Y Zhang, ZM Gibbs, AS Cavanagh, RG Yang, YC Lee, and SM George. Al2o3 and tio2 atomic layer deposition on copper for water corrosion resistance. *ACS applied materials & interfaces*, 3(12):4593–4601, 2011.

[19] GX Shen, YC Chen, and CJ Lin. Corrosion protection of 316 l stainless steel by a tio 2 nanoparticle coating prepared by sol–gel method. *Thin Solid Films*, 489(1):130–136, 2005.

[20] MK Bera, C Mahata, AK Chakraborty, SK Nandi, Jitendra N Tiwari, Jui-Yi Hung, and CK Maiti. Tio2/geoxny stacked gate dielectrics for ge-mosfets. *Semiconductor Science and Technology*, 22(12):1352, 2007.

[21] Geng Wang, Qiang Wang, Wu Lu, and Jinghong Li. Photoelectrochemical study on charge transfer properties of tio2- b nanowires with an application as humidity sensors. *The Journal of Physical Chemistry B*, 110(43):22029–22034, 2006.

[22] Shu-Juan Bao, Chang Ming Li, Jian-Feng Zang, Xiao-Qiang Cui, Yan Qiao, and Jun Guo. New nanostructured tio2 for direct electrochemistry and glucose sensor applications. *Advanced Functional Materials*, 18(4):591–599, 2008.

[23] Bryce S Richards, Jeffrey E Cotter, Christiana B Honsberg, and Stuart R Wenham. Novel uses of tio/sub 2/in crystalline silicon solar cells. In *Conference Record of the Twenty-Eighth IEEE Photovoltaic Specialists Conference, 2000*, pages 375–378. IEEE, 2000.

[24] J-H Kim, S Lee, and H-S Im. The effect of different ambient gases, pressures, and substrate temperatures on tio 2 thin films grown on si (100) by laser ablation technique. *Applied Physics A: Materials Science & Processing*, 69(7):S629–S632, 1999.

[25] A Bendavid, PJ Martin, and H Takikawa. Deposition and modification of titanium dioxide thin films by filtered arc deposition. *Thin Solid Films*, 360(1):241–249, 2000.

[26] Weilin Guo, Zhiming Lin, Xikui Wang, and Guangzhi Song. Sonochemical synthesis of nanocrystalline tio 2 by hydrolysis of titanium alkoxides. *Microelectronic Engineering*, 66 (1):95–101, 2003.

[27] Masayuki Okuya, Koji Nakade, and Shoji Kaneko. Porous tio 2 thin films synthesized by a spray pyrolysis deposition (spd) technique and their application to dye-sensitized solar cells. *Solar energy materials and solar cells*, 70(4):425–435, 2002.

[28] I Joseph Panneerdoss, S Johnson Jeyakumar, and M Jothibas. Characteristic comparison of tio 2 thin films with an inorganic and organic precursor at different molarities by spray pyrolysis. *International Journal Of Engineering And Science*, 4:15–20, 2014.

[29] M Dj Blešić, ZV Šaponjić, JM Nedeljković, and DP Uskoković. Tio 2 films prepared by ultrasonic spray pyrolysis of nanosize precursor. *Materials letters*, 54(4):298–302, 2002.

[30] RS Sonawane, SG Hegde, and MK Dongare. Preparation of titanium (iv) oxide thin film photocatalyst by sol–gel dip coating. *Materials chemistry and physics*, 77(3):744–750, 2003.

[31] Wenli Yang and Colin A Wolden. Plasma-enhanced chemical vapor deposition of tio 2 thin films for dielectric applications. *Thin Solid Films*, 515(4):1708–1713, 2006.

[32] Hongfu Sun, Chengyu Wang, Shihong Pang, Xiping Li, Ying Tao, Huajuan Tang, and Ming Liu. Photocatalytic tio 2 films prepared by chemical vapor deposition at atmosphere pressure. *Journal of Non-Crystalline Solids*, 354(12):1440–1443, 2008.

[33] Sang-Chul Jung, Sun-Jae Kim, Nobuyuki Imaishi, and Yong-Ick Cho. Effect of tio 2 thin film thickness and specific surface area by low-pressure metal–organic chemical vapor deposition on photocatalytic activities. *Applied Catalysis B: Environmental*, 55(4):253–257, 2005.

[34] Samuel Chen, MG Mason, HJ Gysling, GR Paz-Pujalt, TN Blanton, T Castro, KM Chen, CP Fictorie, WL Gladfelter, A Franciosi, et al. Ultrahigh vacuum metalorganic chemical vapor deposition growth and in situ characterization of epitaxial tio2 films. *Journal of Vacuum Science & Technology A: Vacuum, Surfaces, and Films*, 11(5):2419–2429, 1993.

[35] N Rausch and EP Burte. Thin tio2 films prepared by low pressure chemical vapor deposition. *Journal of the Electrochemical Society*, 140(1):145–149, 1993.

[36] P Löbl, M Huppertz, and D Mergel. Nucleation and growth in tio2 films prepared by sputtering and evaporation. *Thin solid films*, 251(1):72–79, 1994.

[37] Rajesh Kumar, Narinder Arorab, and Navjeet Sharmac. Study of spin coated titanium dioxide films. *International Journal of Pure and Applied Physics*, 13(1):229–231, 2017.

[38] MH Suhail, G Mohan Rao, and SDCJ Mohan. dc reactive magnetron sputtering of titanium-structural and optical characterization of tio2 films. *Journal of Applied Physics*, 71(3):1421–1427, 1992.

[39] Abu Z Sadek, Haidong Zheng, Kay Latham, Wojtek Wlodarski, and Kourosh Kalantar-Zadeh. Anodization of ti thin film deposited on ito. *Langmuir*, 25(1):509–514, 2008.

[40] K Bange, CR Ottermann, O Anderson, U Jeschkowski, M Laube, and R Feile. Investigations of tio2 films deposited by different techniques. *Thin solid films*, 197(1-2):279–285, 1991.

[41] Peisheng Liu, Weiping Cai, Ming Fang, Zhigang Li, Haibo Zeng, Jinlian Hu, Xiangdong Luo, and Weiping Jing. Room temperature synthesized rutile tio2 nanoparticles induced by laser ablation in liquid and their photocatalytic activity. *Nanotechnology*, 20(28):285707, 2009.

[42] Mikko Ritala, Markku Leskela, and Eero Rauhala. Atomic layer epitaxy growth of titanium dioxide thin films from titanium ethoxide. *Chemistry of materials*, 6(4):556–561, 1994.

[43] Seigo Ito, Peter Chen, Pascal Comte, Mohammad Khaja Nazeeruddin, Paul Liska, Péter Péchy, and Michael Grätzel. Fabrication of screen-printing pastes from tio2 powders for dye-sensitised solar cells. *Progress in photovoltaics: research and applications*, 15(7):603–612, 2007.

[44] Thomas Siefke, Stefanie Kroker, Kristin Pfeiffer, Oliver Puffky, Kay Dietrich, Daniel Franta, Ivan Ohlídal, Adriana Szeghalmi, Ernst-Bernhard Kley, and Andreas Tünnermann. Materials pushing the application limits of wire grid polarizers further into the deep ultraviolet spectral range. *Advanced Optical Materials*, 4(11):1780–1786, 2016.

[45] Jan Kischkat, Sven Peters, Bernd Gruska, Mykhaylo Semtsiv, Mikaela Chashnikova, Matthias Klinkmüller, Oliana Fedosenko, Stephan Machulik, Anna Aleksandrova, Gregorii Monastyrskyi, et al. Mid-infrared optical properties of thin films of aluminum oxide, titanium dioxide, silicon dioxide, aluminum nitride, and silicon nitride. *Applied optics*, 51(28): 6789–6798, 2012.

[46] Farnood Khalilzadeh-Rezaie, Isaiah O Oladeji, Gbadebo T Yusuf, Janardan Nath, Nima Nader, Shiva Vangala, Justin W Cleary, Winston V Schoenfeld, and Robert E Peale. Optical and electrical properties of tin oxide-based thin films prepared by streaming process for electrodeless electrochemical deposition. *MRS Online Proceedings Library Archive*, 1805, 2015.

[47] Robert E Peale, Evan Smith, Hussain Abouelkhair, Isaiah O Oladeji, Shiva Vangala, Tim Cooper, Gordon Grzybowski, Farnood Khalilzadeh-Rezaie, and Justin W Cleary. Electrodynamic properties of aqueous spray-deposited sno2: F films for infrared plasmonics. *Optical Engineering*, 56(3):037109–037109, 2017.

[48] Janardan Nath, Sushrut Modak, Imen Rezadad, Deep Panjwani, Farnood Rezaie, Justin W Cleary, and Robert E Peale. Far-infrared absorber based on standing-wave resonances in metal-dielectric-metal cavity. *Optics express*, 23(16):20366–20380, 2015.

[49] Farnood K Rezaie, Chris J Fredericksen, Walter R Buchwald, Justin W Cleary, Evan M Smith, Imen Rezadad, Janardan Nath, Pedro Figueiredo, Monas Shahzad, Javaneh Boroumand, et al. Planar integrated plasmonic mid-ir spectrometer. *MRS Online Proceedings Library Archive*, 1510, 2013.

[50] MM Vijatović, JD Bobić, and BD Stojanović. History and challenges of barium titanate: Part ii. *Science of Sintering*, 40(3):235–244, 2008.

[51] Genc Hyseni, Nebi Caka, and Kujtim Hyseni. Analysis of mwir infrared pyroelectric detectors parameters. *Adv. Res. Phys. Eng*, 25:162–165, 2010.

[52] Sea-Fue Wang, Yung-Fu Hsu, Yu-Wen Hung, and Yi-Xin Liu. Effect of ta2o5 and nb2o5 dopants on the stable dielectric properties of batio3–(bi0. 5na0. 5) tio3-based materials. *Applied Sciences*, 5(4):1221–1234, 2015.

[53] Pingsheng Tang, DJ Towner, T Hamano, AL Meier, and BW Wessels. Electrooptic modulation up to 40 ghz in a barium titanate thin film waveguide modulator. *Optics express*, 12(24): 5962–5967, 2004.

[54] FA Yildirim, C Ucurum, RR Schliewe, W Bauhofer, RM Meixner, H Goebel, and W Krautschneider. Spin-cast composite gate insulation for low driving voltages and memory effect in organic field-effect transistors. *Applied physics letters*, 90(8):083501, 2007.

[55] Daniel Hernandez Cruz and Roger A Lessard. Batio3 thin films fabricated by sol-gel process. In *International Symposium on Optical Science and Technology*, pages 9–16. International Society for Optics and Photonics, 2002.

[56] Lev Davidovich Landau, Evgeníj Míkhaílovítsj Lífshíts, and LP Pitaevskii. *Electrodynamics of continuous media*, volume 8. Pergamon press Oxford, 1984.

[57] L Simon-Seveyrat, A Hajjaji, Y Emziane, B Guiffard, and D Guyomar. Re-investigation of synthesis of batio 3 by conventional solid-state reaction and oxalate coprecipitation route for piezoelectric applications. *Ceramics international*, 33(1):35–40, 2007.

[58] F Amy, A Wan, A Kahn, FJ Walker, and RA McKee. Surface and interface chemical composition of thin epitaxial srtio 3 and batio 3 films: Photoemission investigation. *Journal of applied physics*, 96(3):1601–1606, 2004.

[59] Chang-Tai Xia, Er-Wei Shi, Wei-Zhuo Zhong, and Jing-Kun Guo. Preparation of batio3 by the hydrothermal method. *Journal of the European Ceramic Society*, 15(12):1171–1176, 1995.

[60] Margarita García-Hernández, Antonieta García-Murillo, Felipe de J Carrillo-Romo, David Jaramillo-Vigueras, Geneviève Chadeyron, Elder De la Rosa, and Damien Boyer. Eu-doped batio3 powder and film from sol-gel process with polyvinylpyrrolidone additive. *International journal of molecular sciences*, 10(9):4088–4101, 2009.

[61] Kyo Kwang Lee, Yun Chan Kang, Kyeong Youl Jung, and Jung Hyun Kim. Preparation of nano-sized batio 3 particle by citric acid-assisted spray pyrolysis. *Journal of alloys and compounds*, 395(1):280–285, 2005.

[62] Adelina Ianculescu, Sophie Guillemet-Fritsch, and Bernard Durand. Batio3 thick films obtained by tape casting from powders prepared by the oxalate route. *Processing and Application of Ceramics*, 3(1-2):65–71, 2009.

[63] Yasuhisa Yamashita, Hiroshi Yamamoto, and Yukio Sakabe. Dielectric properties of batio3

thin films derived from clear emulsion of well-dispersed nanosized batio3 particles. *Japanese journal of applied physics*, 43(9S):6521, 2004.

[64] EJH Lee, FM Pontes, ER Leite, Elson Longo, José Arana Varela, EB Araujo, and JA Eiras. Preparation and properties of ferroelectric batio3 thin films produced by the polymeric precursor method. *Journal of materials science letters*, 19(16):1457–1459, 2000.

[65] CN George, JK Thomas, HP Kumar, MK Suresh, VR Kumar, PRS Wariar, R Jose, and J Koshy. Characterization, sintering and dielectric properties of nanocrystalline barium titanate synthesized through a modified combustion process. *Materials Characterization*, 60 (4):322–326, 2009.

[66] Christopher J Fredricksen, Justin W Cleary, Walter R Buchwald, Pedro Figueiredo, Farnood Khalilzadeh-Rezaie, Gautam Medhi, Imen Rezadad, Monas Shahzad, Mehmet Yesiltas, Janardan Nath, et al. Planar integrated plasmonic mid-ir spectrometer. In *SPIE Defense, Security, and Sensing*, pages 835321–835321. International Society for Optics and Photonics, 2012.

[67] Farnood Khalilzadeh-Rezaie, Isaiah O Oladeji, Gbadebo T Yusuf, Janardan Nath, Nima Nader, Shiva Vangala, Justin W Cleary, Winston V Schoenfeld, and Robert E Peale. Optical and electrical properties of tin oxide-based thin films prepared by streaming process for electrodeless electrochemical deposition. *MRS Online Proceedings Library Archive*, 1805, 2015.

[68] Farnood Khalilzadeh-Rezaie, Isaiah O Oladeji, Justin W Cleary, Nima Nader, Janardan Nath, Imen Rezadad, and Robert E Peale. Fluorine-doped tin oxides for mid-infrared plasmonics. *Optical Materials Express*, 5(10):2184–2192, 2015.

[69] Sarmad Fawzi Hamza Alhasan, Hussain Abouelkhair, Robert E Peale, and Isaiah O Oladeji. Batio3 film grown by water-based process. *ECS Transactions*, 72(2):343–349, 2016.

[70] Marc Daglish. A dynamic method for determining the pyroelectric response of thin films. *Integrated Ferroelectrics*, 22(1-4):473–488, 1998.

[71] Charles Baldwin Sawyer and CH Tower. Rochelle salt as a dielectric. *Physical review*, 35(3): 269, 1930.

[72] H Tang, H Berger, PE Schmid, and F Levy. Optical properties of anatase (tio2). *Solid State Communications*, 92(3):267–271, 1994.

[73] Jacques I. Pankove. *Optical Processes in Semiconductors*. Dover, New York, 1971. Chapter Three.

[74] T. S. Moss. *Optical Properties of Semiconductors*. Butterworths Scientific Publication LTD.London, 1959.

[75] H Tang, K Prasad, R Sanjines, PE Schmid, and F Levy. Electrical and optical properties of tio2 anatase thin films. *Journal of Applied Physics*, 75(4):2042–2047, 1994.

[76] Hirofumi Takikawa, Takaaki Matsui, Tateki Sakakibara, Avi Bendavid, and Philip J Martin. Properties of titanium oxide film prepared by reactive cathodic vacuum arc deposition. *Thin Solid Films*, 348(1):145–151, 1999.

[77] GK Boschloo, A Goossens, and J Schoonman. Photoelectrochemical study of thin anatase tio2 films prepared by metallorganic chemical vapor deposition. *Journal of The Electrochemical Society*, 144(4):1311–1317, 1997.

[78] Akihiko Aoki and Gyoichi Nogami. Fabrication of anatase thin films from peroxo-polytitanic acid by spray pyrolysis. *Journal of The Electrochemical Society*, 143(9):L191–L193, 1996.

[79] Zhongchun Wang, Ulf Helmersson, and Per-Olov Käll. Optical properties of anatase tio 2 thin films prepared by aqueous sol–gel process at low temperature. *Thin Solid Films*, 405(1): 50–54, 2002.

[80] Janardan Nath, Deep Panjwani, Farnood Khalilzadeh-Rezaie, Mehmet Yesiltas, Evan M Smith, James C Ginn, David J Shelton, Carol Hirschmugl, Justin W Cleary, and Robert E Peale. Infra-red spectral microscopy of standing-wave resonances in single metal-dielectric-metal thin-film cavity. In *SPIE Nanoscience+ Engineering*, pages 95442M–95442M. International Society for Optics and Photonics, 2015.

[81] RJ Gonzalez, R Zallen, and H Berger. Infrared reflectivity and lattice fundamentals in anatase tio 2 s. *Physical Review B*, 55(11):7014, 1997.

[82] AL Patterson. The scherrer formula for x-ray particle size determination. *Physical review*, 56(10):978, 1939.

[83] Igor Lubomirsky and Oscar Stafsudd. Invited review article: Practical guide for pyroelectric measurements a. *Review of Scientific Instruments*, 82(5):121101, 2012.

[84] WH Zachariasen and C Kittel. Introduction to solid state physics. 1956.